The EUMETSAT Network of Satellite Application Facilities

NWC SAF
Support to Nowcasting and Very Short Range Forecasting

Scientific and Validation Report for the "Automatic Satellite Image Interpretation – Next Generation" Processors of the NWC/GEO

NWC/CDOP3/GEO/ZAMG/SCI/VR/ASII-NG, Issue 1.0

21 January 2019

Applicable to

GEO-ASII-NG-v2.0 (NWC-048)

which is comprised of

GEO-ASII-GW-v1.0

GEO-ASII-TF-v2.0

Prepared by ZAMG

REPORT SIGNATURE TABLE

Function	Name	Signature	Date
Prepared by	A. Jann (ZAMG) for ASII-GW, A. Wirth (ZAMG) for ASII-TF		*21 January 2019*
Reviewed by	A. Jann (ZAMG) for ASII-TF, A. Wirth (ZAMG) for ASII-GW		*21 January 2019*
Authorised by	Pilar Rípodas, AEMET *SAFNWC Project Manager*		*21 January 2019*

DOCUMENT CHANGE RECORD

Version	Date	Pages	CHANGE(S)
1.0	*21 January 2019*	51	Creation

Table of contents

1. INTRODUCTION 9

1.1 SCOPE AND PURPOSE OF THE DOCUMENT 9
1.2 DEFINITIONS, ACRONYMS AND ABBREVIATIONS 9
1.3 REFERENCES 11
1.3.1 Applicable Documents 11
1.3.2 Reference Documents 11

2. VALIDATION OF THE ASII-NG GRAVITY WAVE PRODUCT, V1.0 12

2.1 BACKGROUND AND SCOPE 12
2.2 INITIAL ASSESSMENTS 13
2.3 RESULTS 15
2.3.1 29 June 2017, 1400 UTC 16
2.3.2 29 June 2017, 1630 UTC 25
2.4 CONCLUSIONS 26
2.5 LAST-MINUTE UPDATES 27
2.6 REFERENCED SCIENTIFIC PUBLICATIONS 29

3. VALIDATION OF THE ASII-NG TROPOPAUSE FOLD PRODUCT, V2.0 30

3.1 VALIDATION OF THE ASII-TF PRODUCT AGAINST PIREPS 30
3.2 COMPARING THE ASII-TF OUTPUT AGAINST IASI LEVEL 2 DERIVED TROPOPAUSE FOLDS 36
3.3 CASE STUDY: 16 APRIL 2018 39
3.3.1 Synoptic situation 40
3.3.2 Comparison of ASII-TF with IASI level 2 tropopause height 42
3.3.3 Evaluation of the PIREPs (16 April 2018) 44
3.4 CONCLUSIONS 50
3.5 REFERENCED SCIENTIFIC PUBLICATIONS 51

List of tables

Table 1: List of Applicable Documents 11

Table 2: List of Referenced Documents 11

Table 3: Number of all turbulence reports as a function of their intensity and their assigned ASII-TF probability (LGT: light, MOD: moderate and SEV: severe). 32

Table 4: Number of turbulence reports caused by strong vertical wind shear as a function of their intensity and their assigned ASII-TF probability (LGT: light, MOD: moderate and SEV: severe). 33

Table 5: Number of turbulence reports associated with strong curvature of the wind trajectory (green), by vertical wind shear resulting from velocity (orange) and by directional shear (blue) as a function of their assigned ASII-TF probability. 35

List of figures

Figure 1: Appearance of gravity waves in the lee of mountain ranges, case of 25 January 2014, 1200 UTC. Upper panel: Meteosat-10 high-resolution visible image, showing lee wave clouds at the northern coasts of Spain and Algeria. The signature of these gravity waves can be seen in the WV7.3 image as well (lower panel), albeit generally blurred due to the lower spatial resolution (conversely, the wavy appearance over Tunisia is much clearer depicted in the WV channel than in the cloud image). 12

Figure 2: Case of 27 October 2017, 1230 UTC. Uppermost panel: The probability-of-occurrence of gravity waves, as analysed by the respective ASII-NG module, v2017, on the basis of the WV7.3 image (the colour table runs from dark blue = 0% to red=100%;the black areas are those masked by a temperature threshold used to avoid random signals in thick clouds; the signal over Greece actually is due to such a random hit that barely escaped the temperature filtering, accidentally satisfying the mathematical criteria for one image and disappearing in the next). Middle panel: Excerpt of the used WV7.3 image. Lower panel: The corresponding HRVIS image. 15

Figure 3: Case of 29 June 2017, 1400 UTC, Northern hemisphere. Upper panel: The METEOSAT WV7.3 image. Lower panel: The ASII-NG probability-of-gravity-wave product; same colour table as in **Figure 2**: 0% areas in dark blue; 100% probability signalled in red; here the areas masked by the temperature threshold to avoid random signals in thick clouds are shown in white. 16

Figure 4: Same as **Figure 3**, but for the southern hemisphere. 17

Figure 5: A zoomed portion of the WV7.3 image of **Figure 4**. 18

Figure 6: A zoomed portion of the WV7.3 image of **Figure 4**, southernmost Africa. The superimposed cyan lines are those along which the detection algorithm, v2017, found a grating pattern. The ripples clearly seen from the southwestern corner of South Africa landwards have been poorly detected. 19

Figure 7: Same as **Figure 6** but the detection algorithm run for the twofold number of angles... 19

Figure 8: Same as **Figure 6** but the detection algorithm being less restrictive on the minimum accepted signal. 20

Figure 9: Upper panel: A European portion of the WV7.3 image of **Figure 3**. Cyan crosses mark gravity wave regions deserving particular attention. Lower panel: Same image, with superimposed cyan lines showing the results of the grating detection with the "operational" parameter setting of v2017. 20

Figure 10: As **Figure 9**, but the superimposed results are from runs with twofold number of angles (upper panel) and looser restriction (ΔT=0.1 K) on minimum signal (lower panel)... 21

Figure 11: A southern African portion of the WV7.3 image of **Figure 4**. The superimposed cyan lines are those along which the detection algorithm found a grating pattern. 22

Figure 12: Upper panel: A zoomed portion of the WV7.3 image of **Figure 4** (over Spain). Lower panel: Simultaneously recorded Meteosat-10 high-resolution visible imagery. The -1.5-units isoline of the Gabor filter field with λ=4 pixels, Θ=15π/16 is superimposed in order to establish the connection between the ripples seen in the WV image and the structures shown in this HRVIS image. 23

Figure 13: Upper panel: Meteosat-10 7.3µm water vapour image recorded over the Iberian peninsula on 29 June 2017, 0000 UTC, showing widespread gravity wave ripple signatures in the northern and eastern sectors. Lower panel: The simultaneously recorded Meteosat-10 10.8 µm infrared image. 24

Figure 14: Case of 29 June 2017, 1630 UTC, Northern hemisphere. Upper panel: The ASII-NG probability-of-gravity-wave product based on the MSG-1 WV7.3 image. Lower panel: The ASII-NG probability-of-gravity-wave product based on the MSG-3 WV7.3 image. Colour table as in **Figure 2**: areas with 0% probability in dark blue; 100% probability signalled in red; the areas masked by the temperature threshold to avoid random signals in thick clouds are shown in white..... 26

Figure 15: Same as **Figure 14**, but for the southern hemisphere. 26

Figure 16: The WV7.3 image of 29 June 2017, 1400 UTC, South Africa and surrounding ocean, superimposed by the 1, 50 and 99% isolines of probability of gravity-wave occurrence, as indicated by the ASII-GW product, v2018..... 27

Figure 17: The WV7.3 image of 29 June 2017, 1400 UTC, over Mediterranean Europe, superimposed by the 1, 50 and 99% isolines of probability of gravity-wave occurrence, as indicated by the ASII-GW product, v2018..... 28

Figure 18: The WV7.3 image of 29 June 2017, 1400 UTC, over Botswana, superimposed by the 1, 50 and 99% isolines of probability of gravity-wave occurrence, as indicated by the ASII-GW product, v2018. 28

Figure 19: The blue line delimits the area of the ASII-TF analysis used in this evaluation. 31

Figure 20: Example of Pilot Reports (black dots) and associated text lines of the Pilot Report located on the ASII-TF product. Date: 29 April 2018, 06:00 UTC. 32

Figure 21: ASII-TF product from 24 June 2018 at 20:45 UTC. The indicated PIREP position (black dot) lies in the green area of medium probability values and near to the red zone of high probability values of being at a tropopause fold. 34

Figure 22: ASII-TF product from 6 June 2018 at 14:00 UTC. Convective cells are depicted with a low probability for being located near a tropopause fold (red: high probability, green: medium probability and blue: low probability)..... 34

Figure 23: Scatterplot of IASI level-2 tropopause gradient versus ASII-TF probabilities for 22 March 2018, 09:00 UTC overpass. The red line depicts the linear regression line; the correlation coefficient is 0.52. 37

Figure 24: Comparison of the IASI derived tropopause folds (right) with the ASII-TF output (left). Date: 26 March 2018, 20:45 UTC. High probabilities for being located at a tropopause fold are depicted in red in the ASII-TF product; high gradients of the tropopause height are depicted in green in the IASI output. 37

Figure 25: Comparison of the IASI-derived tropopause folds (right) with the ASII-TF output (left). Date: 27 March 2018, 08:45 UTC. High probabilities for being located at a tropopause fold are depicted in red in the ASII-TF product; high gradients of the tropopause height are depicted in green in the IASI output. 38

Figure 26: Comparison of the IASI-derived tropopause folds (bottom right) with the ASII-TF output (bottom left). Date: 27 March 2018, 08:45 UTC. High probabilities for being located at a tropopause fold are depicted in red in the ASII-TF product; high gradients of the tropopause height are depicted in green in the IASI output. IR 10.8 µm (top left) and WV 6.2 µm (top right) images from Meteosat-11 show the position of the large convective cell. 39

Figure 27: GFS analysis for 16 April 2018 at 00:00 UTC indicating geopotential heights at 500 hPa and surface pressure (white). 40

Figure 28: DWD surface chart for 16 April 2018, 00:00 UTC. The area of interest is marked in green. 41

Figure 29: IR10.8 µm satellite image from Meteosat-11 (16 April 2018, 00:00 UTC); isotachs at 300 hPa in yellow and wind direction in green. The red line marks the axis of the jet streak. 42

Figure 30: Left: ASII-TF analysis for 16 April 2018, 08:45 UTC. Areas with a high probability for being located at a tropopause fold are marked in red. Right: Tropopause gradient from IASI sounding data for the same day at 08:50 UTC. 43

Figure 31: IR10.8 µm satellite image from Meteosat-11 (16 April 2018, 06:00 UTC); isotachs at 300 hPa in yellow and wind direction in green. The red line marks the axis of the jet streak. 43

Figure 32: Detail of the ASII-TF product for 16 April 2018, 12:15 UTC. Areas with a high probability for being located at a tropopause fold are marked in red. PIREPS and their exact locations are marked in black. 44

Figure 33: 16 April 2018, 12:00 UTC: Vertical cross section through the area of the reported turbulence. The position of the cross section is marked in green; isotachs at the 300 hPa level are depicted in yellow. 45

Figure 34: Detail of the ASII-TF product for 16 April 2018, 13:15 UTC. Areas with a high probability for being located at a tropopause fold are marked in red. PIREPS and their exact locations are marked in black. 46

Figure 35: Detail of the ASII-TF product for 16 April 2018, 14:00 UTC. Areas with a high probability for being located at a tropopause fold are marked in red. PIREPS and their exact locations are marked in black. 46

Figure 36: IR 10.8 µm image from Meteosat-11 (16 April 2018, 14:00 UTC). The black dot marks the area of the reported turbulence, developing Cumulonimbus clouds are indicated by orange Cb tags. 47

Figure 37: Detail of the ASII-TF product for 16 April 2018, 14:30 UTC. Areas with a high probability for being located at a tropopause fold are marked in red. PIREPS and their exact locations are marked in black. 47

Figure 38: Detail of the ASII-TF product for 16 April 2018, 15:30 UTC. Areas with a high probability for being located at a tropopause fold are marked in red. PIREPS and their exact locations are marked in black. 48

Figure 39: Detail of the ASII-TF product for 16 April 2018, 16:00 UTC. Areas with a high probability for being located at a tropopause fold are marked in red. PIREPS and their exact locations are marked in black. 49

Figure 40: NWCSAF Cloud top height and surface weather reports from 16 April 2018 at 16:00 UTC. 49

Figure 41: 16 April 2018, 18:00 UTC: Vertical cross section through the area of the reported turbulence. The red circles indicate the location of the reported moderate to severe turbulence. 50

1. INTRODUCTION

The EUMETSAT's "Satellite Application Facilities" (SAFs) are dedicated centres of excellence for processing satellite data, and form an integral part of the distributed EUMETSAT Application Ground Segment (http://www.eumetsat.int). This documentation is provided by the SAF on Support to Nowcasting and Very Short Range Forecasting, NWCSAF. The main objective of NWCSAF is to provide, further develop and maintain software packages to be used for Nowcasting applications of operational meteorological satellite data by National Meteorological Services. More information can be found at the NWC SAF webpage, http://nwc-saf.eumetsat.int.

1.1 SCOPE AND PURPOSE OF THE DOCUMENT

This document is the first Validation Report for the gravity wave detection sub-product (ASII-GW) of the NWC/GEO Automatic Satellite Interpretation – Next Generation Product (PGE17, ASII-NG, NWC/GEO release 2018) (chapter 2) and the Validation Report for v2.0 of the tropopause fold detection sub-product (ASII-TF) (chapter 3).

This document contains a description of the validation methods and the corresponding results for the above-mentioned sub-products.

1.2 DEFINITIONS, ACRONYMS AND ABBREVIATIONS

ASII	Automatic Satellite Image Interpretation
ASII-GW	Gravity wave detection sub-product of ASII-NG
ASII-NG	Automatic Satellite Image Interpretation – Next Generation
ASII-TF	Tropopause fold detection sub-product of ASII-NG
ATBD	Algorithm Theoretical Baseline Document
EUMETSAT	European Organisation for the Exploitation of Meteorological Satellites
FL	Flight Level
GW	Gravity wave(s)
IR	Infrared
IASI	Infrared Atmospheric Sounding Instrument
LGT	Light (turbulence)
MetOp	Meteorological Operational Satellite
MOD	Moderate (turbulence)
MSG	Meteosat Second Generation
NWCSAF	SAF to support NoWCasting and Very-Short-Range Forecasting
NWP	Numerical Weather Prediction
PIREP	Pilot Report
PGE	Product Generation Element
SAF	Satellite Application Facility

SEV	Severe (turbulence)
SEVIRI	Spinning Enhanced Visible and Infrared Imager
SW	Software
WV	Water Vapour

1.3 REFERENCES

1.3.1 Applicable Documents

The following documents, of the exact issue shown, form part of this document to the extent specified herein. Applicable documents are those referenced in the Contract or approved by the Approval Authority. They are referenced in this document in the form [AD.X].

For dated references, subsequent amendments to, or revisions of, any of these publications do not apply. For undated references, the current edition of the document referred applies.

Current documentation can be found at the NWC SAF Helpdesk web: http://nwc-saf.eumetsat.int.

Ref	Title	Code	Vers	Date
[AD.1]	Project Plan for the NWCSAF CDOP3 phase	NWC/CDOP3/SAF/AEMET/MGT/PP	1.0	06/03/18
[AD.2]	NWCSAF CDOP3 Project Plan Master Schedule	NWC/CDOP3/SAF/AEMET/MGT/PP/MasterSchedule	1.1	28/02/18
[AD.3]	Configuration Management Plan for the NWC SAF	NWC/CDOP3/SAF/AEMET/MGT/CMP	1.0	21/02/18
[AD.4]	System and Components Requirements Document for the NWC/GEO	NWC/CDOP2/GEO/AEMET/SW/SCRD	2.1	21/01/19
[AD.5]	Interface Control Document for Internal and External Interfaces of the NWC/GEO	NWC/CDOP3/GEO/AEMET/SW/ICD/1	1.0	21/01/19
[AD.6]	Interface Control Document for the NWCLIB of the NWC/GEO	NWC/CDOP3/GEO/AEMET/SW/ICD/2	1.0	21/01/19
[AD.7]	Data Output Format	NWC/CDOP3/GEO/AEMET/SW/DOF	1.0	21/01/19
[AD.8]	Component Design Document for the NWCLIB of the NWC/GEO	NWC/CDOP2/GEO/AEMET/SW/ACDD/NWCLIB	2.0	27/02/17
[AD.9]	NWC SAF Product Requirements Document	NWC/CDOP3/GEO/AEMET/MGT/PRD	1.0	01/18
[AD.10]	User Manual for the Tools of the NWC/GEO	NWC/CDOP3/GEO/AEMET/SCI/UM/Tools	1.0	21/01/19

Table 1: *List of Applicable Documents*

1.3.2 Reference Documents

The reference documents contain useful information related to the subject of the project. These reference documents complement the applicable ones, and can be looked up to enhance the information included in this document if it is desired. They are referenced in this document in the form [RD.X].

For dated references, subsequent amendments to, or revisions of, any of these publications do not apply. For undated references, the current edition of the document referred applies.

Current documentation can be found at the NWC SAF Helpdesk web: http://nwc-saf.eumetsat.int

Ref	Title	Code	Vers	Date
[RD.1]	The Nowcasting SAF Glossary	NWC/CDOP2/SAF/AEMET/MGT/GLO		
[RD.2]	User Manual for the "Automatic Satellite Image Interpretation – Next Generation" Processors of the NWC/GEO: Science Part	NWC/CDOP2/GEO/ZAMG/SCI/UM/ASII-NG	2.0	21/01/19
[RD.3]	Algorithm Theoretical Baseline Document for the "Automatic Satellite Image Interpretation – Next Generation" Processor of the NWC/GEO	NWC/CDOP2/GEO/ZAMG/SCI/ATBD/ASII-NG	2.1	21/01/19

Table 2: *List of Referenced Documents*

2. VALIDATION OF THE ASII-NG GRAVITY WAVE PRODUCT, V1.0

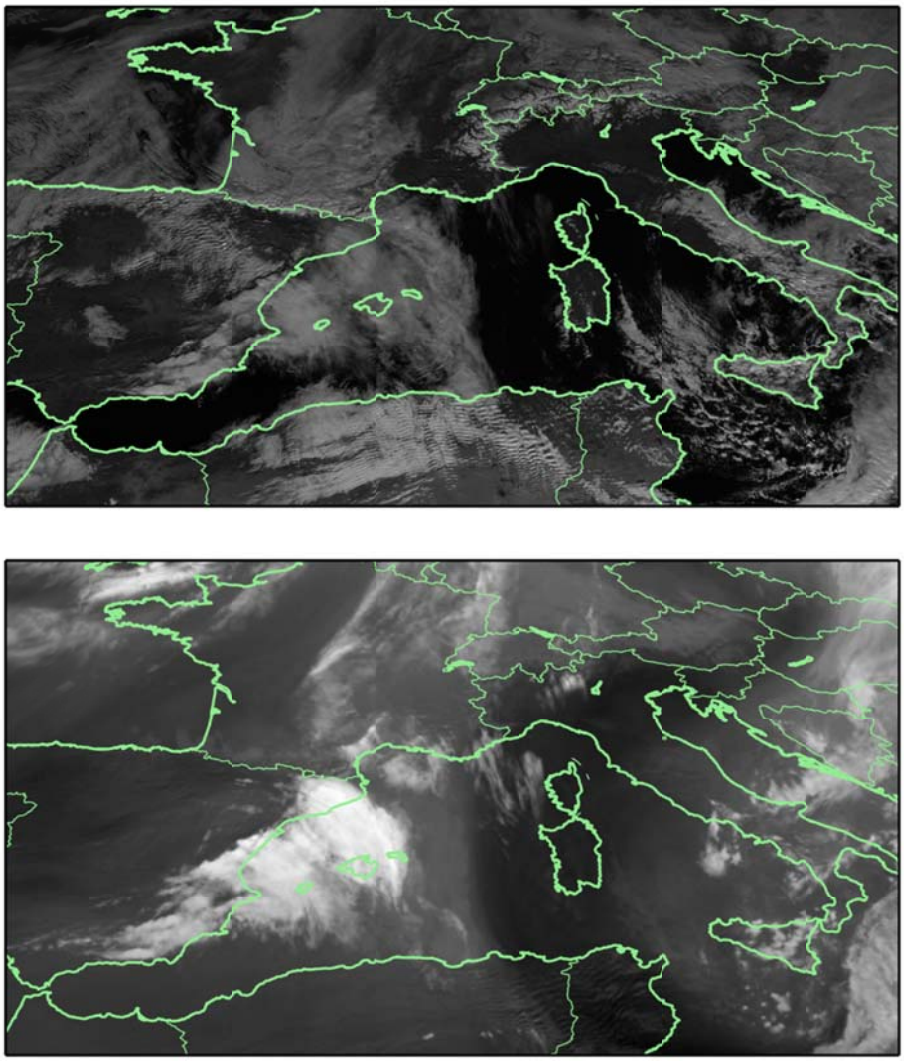

Figure 1: *Appearance of gravity waves in the lee of mountain ranges, case of 25 January 2014, 1200 UTC. Upper panel: Meteosat-10 high-resolution visible image, showing lee wave clouds at the northern coasts of Spain and Algeria. The signature of these gravity waves can be seen in the WV7.3 image as well (lower panel), albeit generally blurred due to the lower spatial resolution (conversely, the wavy appearance over Tunisia is much clearer depicted in the WV channel than in the cloud image).*

2.1 BACKGROUND AND SCOPE

As described in the ASII-NG ATBD [RD.3], this product suite shall comprise modules relevant for aviation meteorology, through objective detection of patterns generally considered as indicative of (clear-air) turbulence (besides the gravity waves considered here, ASII-NG v2018 features a separate module dealing with tropopause folds). Though the significance of those features is commonly acknowledged among aviation meteorologists, it has to be emphasized that they are just alerting signals but the relation between the meteorological phenomena and the actual consequence in day-to-day aviation is too loose to be exploited for validation purposes: there is no guarantee that an aircraft flying through such a two-dimensionally delineated region must experience turbulence (if it is lucky enough to catch a calm flight level, for example), and

vice versa there can be no guarantee that an occurrence of turbulence is necessarily linked with a meteorological phenomenon discernible in the Meteosat imagery (for a more comprehensive reading about difficulties of verification against PIREPs, the interested reader may like to consult the paper of Brown and Young, 2000). The idea behind the ASII-NG gravity wave product (ASII-GW) consequently is: support the aviation forecaster in making his/her decision (from the meteorological material comprising much more than just the ASII-NG) by relieving him/her from a subjective search over the whole image by providing a reliable objective identification of the relevant pattern.

In the case of ASII-GW, the relevant signal seen in Meteosat imagery are parallel stripes / ripples (see **Figure 1**), and the task of the validation is to give insight how well the outcome of the employed pattern recognition algorithm corresponds with a subjective diagnosis of these patterns. For the sake of completeness, we note that the meteorological literature (e.g. Fritts and Alexander, 2003; Sharman and Lane, 2016) knows

- gravity waves near/above convection (relevant to aviation);
- gravity waves in regions of the middle atmosphere (where no commercial aircraft flies),

but NWC/GEO restricts itself to phenomena that can be seen with reasonable likelihood in Meteosat imagery which keeps those parts of the spectrum out-of-scope here.

2.2 INITIAL ASSESSMENTS

The ASII-NG stripe detection module had its starting point in papers by Kruizinga and Petkov (1995, 1999) and Petkov and Kruizinga (1997) with background far from any meteorological application. Not surprisingly, some tuning of the algorithm was necessary to make it suitable for our purposes, and as tuning and validation are mutually linked, much validation was already undertaken when the first version was presented. This initial validation exercise was performed on a sample of 30 cases of manually analysed gravity waves (these analyses were chiefly based on the HRVIS images; region: Europe). The results of this exercise are available in a peer-reviewed open-source journal (Jann, 2017), so it is sufficient to present just a summary of highlights here:

1) The algorithm looks for alternating bright and dark stripy zones and is very sensitive about this. Essentially, this means that if the meteorologist detects this pattern in the channel under investigation, the algorithm will not miss it.
2) However, as the algorithm is so skillful in detecting the stripe arrangements, we easily get some false alarms in areas where such patterns are not related to gravity waves. The mentioned paper lists snow/no-snow alterations in cloud free Alpine regions and marine stratocumulus. In such situations, the resulting signal is understandable from the algorithmic viewpoint, but with the goal of the ASII-NG product in mind, some measures should be sought in order to suppress them. As this seems to be easier in WV7.3 than e.g. in HRVIS, the decision was to base the first release in NWC/GEO on the WV7.3 channel.

Subsequently, the algorithm in its published form was incorporated in the operational NWCSAF environment at the developer's premises, thus allowing random inspection of the NRT performance. The alert reader may note a subtle change in the meaning of a variable (q') between Eq.(8) in Jann (2017) and the corresponding equation with the same number in the more recent ASII-NG ATBD [RD.3], which occurred during that period. Details should be obtained from the referenced document; may it suffice to note here simply that the transition had already been taken place when we entered the validation exercise described in the following section. The status (for short named "v2017") is illustrated by the example of **Figure 2**, picked randomly from ZAMG's NWC/GEO NRT visualization. Inspection of this picture leads to the conclusions:

- ASII-NG GW appears to be a useful tool to recognize the characteristic ripples in WV 7.3 (which sometimes would even be overlooked by the naked eye if not inspecting the image very thoroughly; in fact, it also took some greyscale manipulation to make them clearly visible here…) – all regions with 100% probability are found to be correct hints to the sought phenomenon.
- Looking at the HRVIS, there are useful complementary signals over Southern France. One has to hope that future work eliminates the false alarms which in HRVIS analyses are too many at present (without showing it in the Figure, we know from our experience that the same analysis applied to the HRVIS would generate a strong signal from the regular patterns arising from the convection over Northern France and the marine stratocumulus in the southeast corner of the image).

As this kind of evaluations was nearing saturation (i.e. the same results were obtained over and over again), it seemed to be prudent at a certain stage to widen the validation area and to go for the full Meteosat disk.

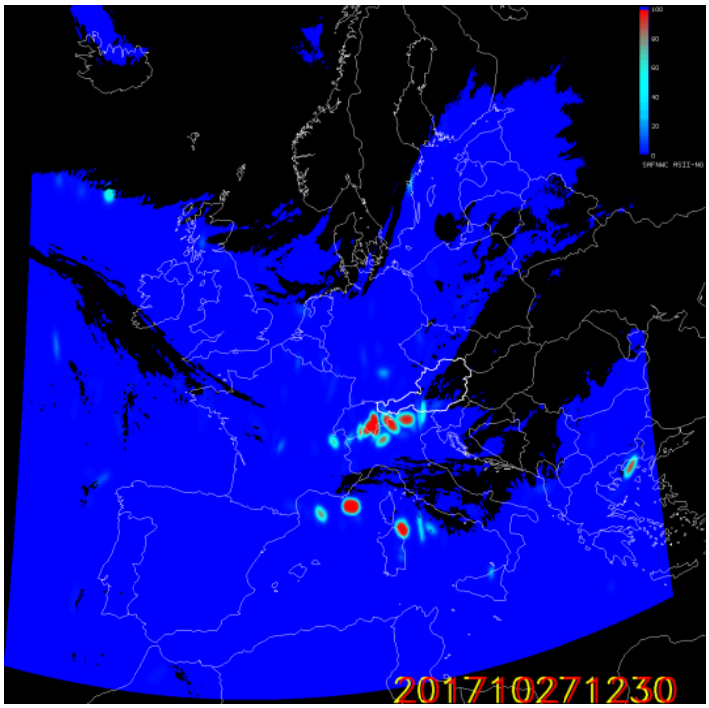

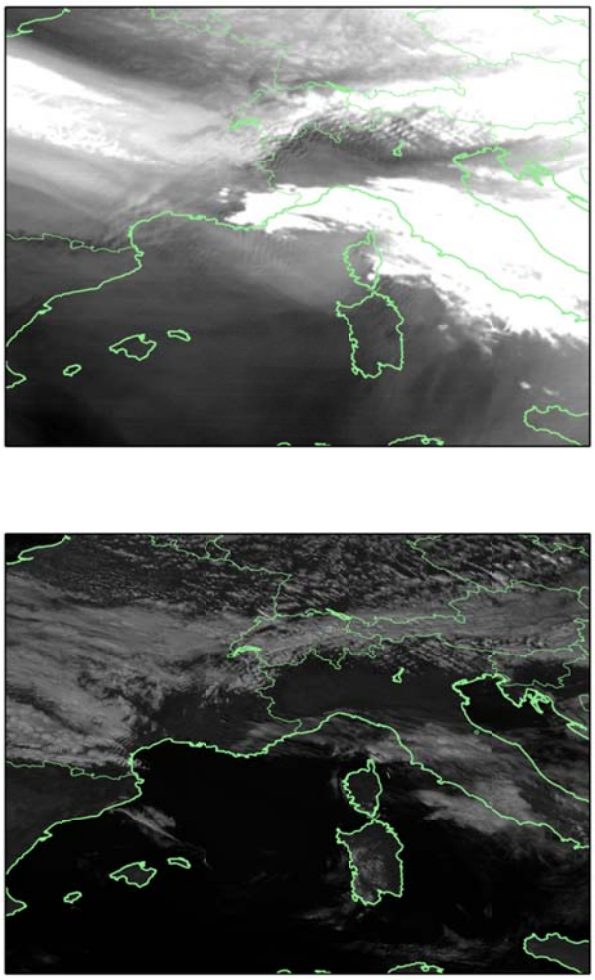

Figure 2: *Case of 27 October 2017, 1230 UTC. Uppermost panel: The probability-of-occurrence of gravity waves, as analysed by the respective ASII-NG module, v2017, on the basis of the WV7.3 image (the colour table runs from dark blue = 0% to red=100%;the black areas are those masked by a temperature threshold used to avoid random signals in thick clouds; the signal over Greece actually is due to such a random hit that barely escaped the temperature filtering, accidentally satisfying the mathematical criteria for one image and disappearing in the next). Middle panel: Excerpt of the used WV7.3 image. Lower panel: The corresponding HRVIS image.*

2.3 RESULTS

This chapter discusses results obtained for the case study of 29 June 2017. The trigger to select this very day was the widespread occurrence of lee waves over Europe on that day, so a considerable sample of events was ensured. However, as announced in the precursor section, subsequently the Meteosat-10 imagery for the whole disk was ordered and processed. As the computations moreover span the whole day, the investigation covered daytime, nighttime, summer and winter situations. There is actually not much reason to expect the detection of a geometric pattern to depend on such factors. However, looking to other regions and different seasons might reveal meteorological situations leading to false alarms that would perhaps not have been discovered in the typical European scene. It will soon be seen that this in fact materialized.

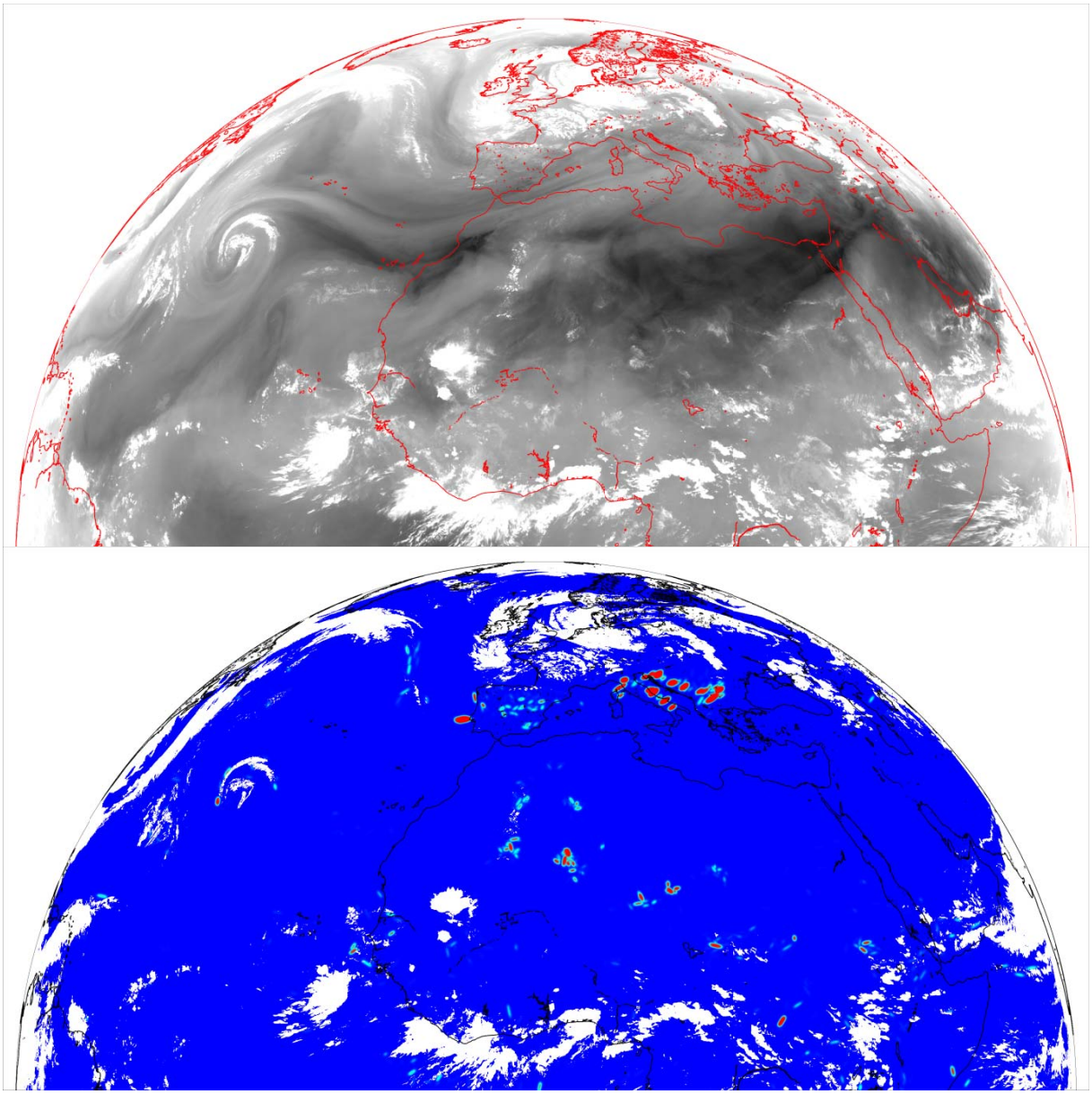

Figure 3: *Case of 29 June 2017, 1400 UTC, Northern hemisphere. Upper panel: The METEOSAT WV7.3 image. Lower panel: The ASII-NG probability-of-gravity-wave product; same colour table as in* ***Figure 2****: 0% areas in dark blue; 100% probability signalled in red; here the areas masked by the temperature threshold to avoid random signals in thick clouds are shown in white.*

2.3.1 29 June 2017, 1400 UTC

Figure 3 and **Figure 4** present the overview over the situation at 1400 UTC, namely the WV7.3 imagery and the ASII-NG gravity wave analysis resulting from it. For validation purposes, it should be sufficient to look at the regions where the gravity wave detection yields large responses (in case the detection algorithm fails to detect waves under certain circumstances, we expect to see this also somewhere in the regions of widespread GW occurrence, hence encountering "no-detection" issues, if there are any).

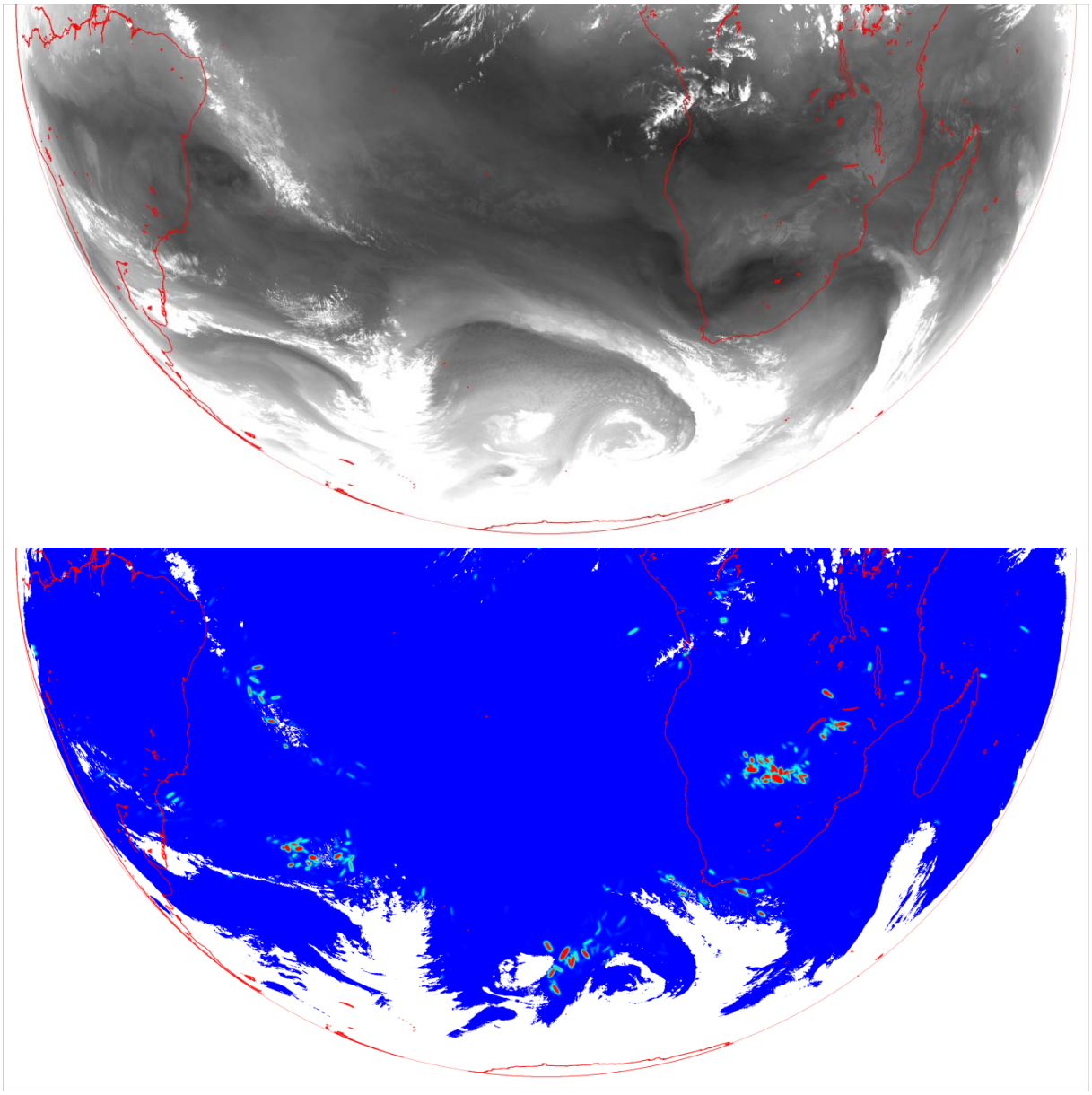

Figure 4: *Same as* ***Figure 3****, but for the southern hemisphere.*

The figures also give an impression how difficult it is to spot gravity wave patterns in a large-scale WV image in standard graphical representation, and thus how welcome an objective analysis tool is. In contrast, the images presented in **Figure 5**ff. underwent some colour enhancement to achieve a clearer visibility in the figures; they therefore give a somewhat distorted image about the situation encountered in operational practice. In particular, the following sections zoom in to 1) the Cape Town region and the Atlantic southwestwards; 2) Mediterranean Europe (Spain – Balkans); 3) the region north of South Africa (~Botswana) exhibiting a cluster of strong signals.

2.3.1.1 Cape Town and southward

A first evaluation result was quickly obtained by zooming in into the Atlantic region southwest of South Africa (***Figure 5***). A field of marine stratocumulus is clearly seen that exhibits such regularity in its features that the algorithm responds at many places. This source of false alarms

was already highlighted in Jann (2017), and the remedy was to introduce the temperature threshold on WV7.3 that leads to the masked regions around Antarctica in the ASII-NG panel of ***Figure 4***. It turns out that the constant threshold (normally working quite well over Europe[1]) does not filter the Stratocumulus in this case. Note that the simple reflex to change the constant threshold to the warmer side would have been an inadequate reaction as it soon discards parts of the image where actual gravity waves are present.

Moving to the northeast, an area of ripples is found in western South Africa (***Figure 6***), for which the detection algorithm gave a disappointingly low number of hits (in particular when compared with the signals in the clouds south of the coast). For this diagram, the algorithm investigates the situation along lines in 8 different angles (separated by $\pi/8$). One might presume that increasing the number of investigated angles might improve the detection rate over South Africa. Going for 16 angles (separated by $\pi/16$), this is (of course) indeed observed but not to a degree that makes the analysis really much more satisfactory and would justify the doubled computation time (also the distinction vis-à-vis the clouds off the coast has not really improved since the number of signals there went up as well. Another screw to turn is the minimum response a pattern should yield for being eligible when convolved with the used Gabor filter. As the ATBD explains in more detail, a certain magnitude of brightness fluctuations ΔT should be reached, and this magnitude was set to 0.4 K in v2017. The outcome of changing this threshold to 0.1 is fairly spectacular, with a high number of (subjectively confirmed) wave detections popping up over most of South Africa, and almost no additions in the areas where we had unwanted signals. Hence, if we go for the density of the hits (which is what the ASII-GW product does to achieve the probability output, Eq. 1), this is now much more favourably leaning towards the pattern we actually want to detect. Comparing ***Figure 6*** and ***Figure 8*** suggests that the wish to suppress false alarms originally led to a too strict setting of the threshold.

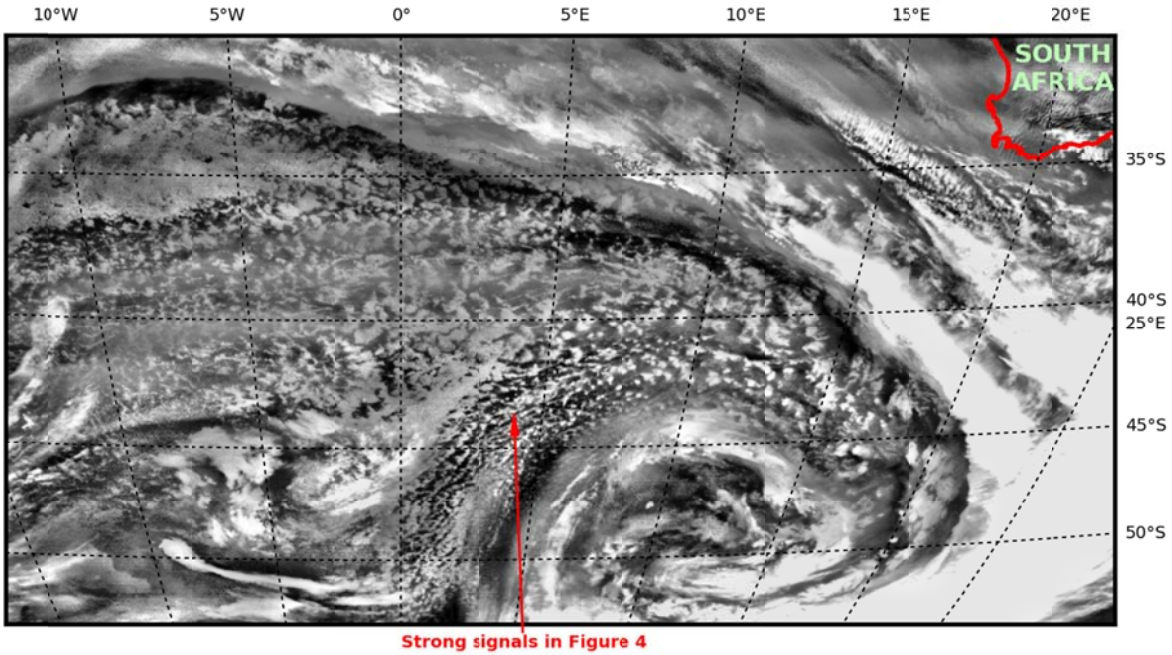

Figure 5: *A zoomed portion of the WV7.3 image of* ***Figure 4****.*

[1] However, sensibilized by the example of ***Figure 5***, we later detected a couple of cases of disturbing marine stratocumulus also in the North Atlantic during the Northern hemisphere winter. Apparently, the marine Sc in the winter season tend to have less water vapour content in the relevant layers, which makes them more difficult to filter.

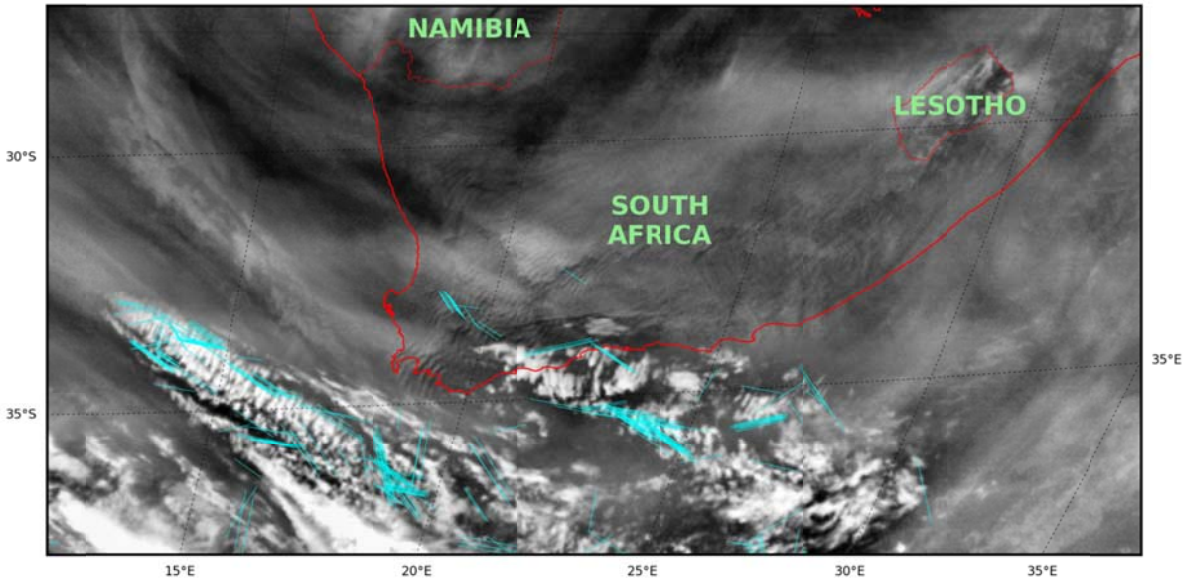

Figure 6: *A zoomed portion of the WV7.3 image of* ***Figure 4****, southernmost Africa. The superimposed cyan lines are those along which the detection algorithm, v2017, found a grating pattern. The ripples clearly seen from the southwestern corner of South Africa landwards have been poorly detected.*

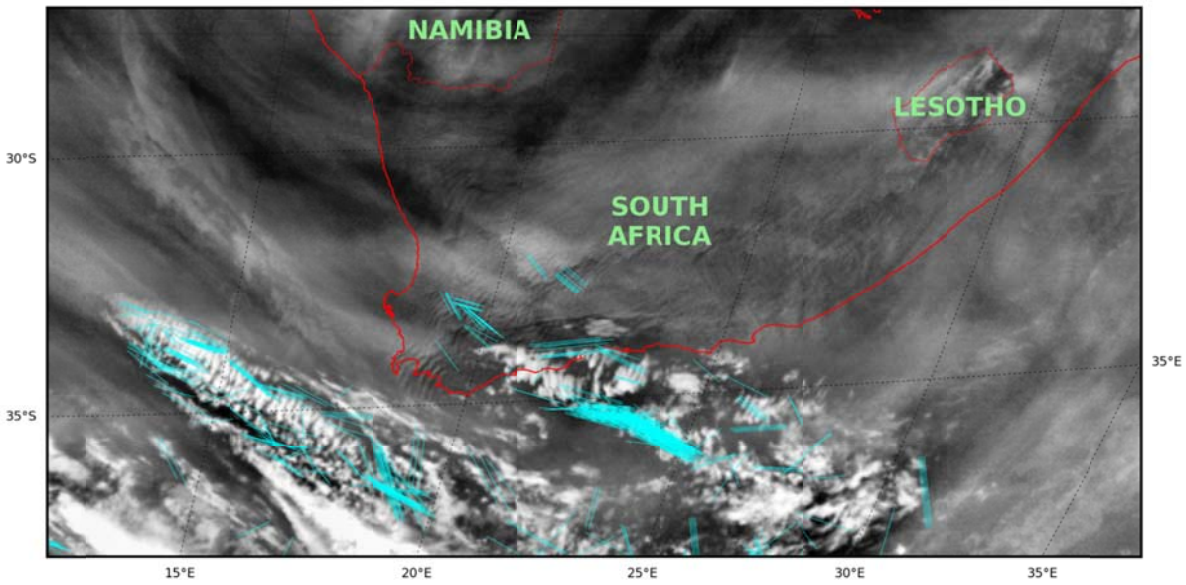

Figure 7: *Same as* ***Figure 6*** *but the detection algorithm run for the twofold number of angles.*

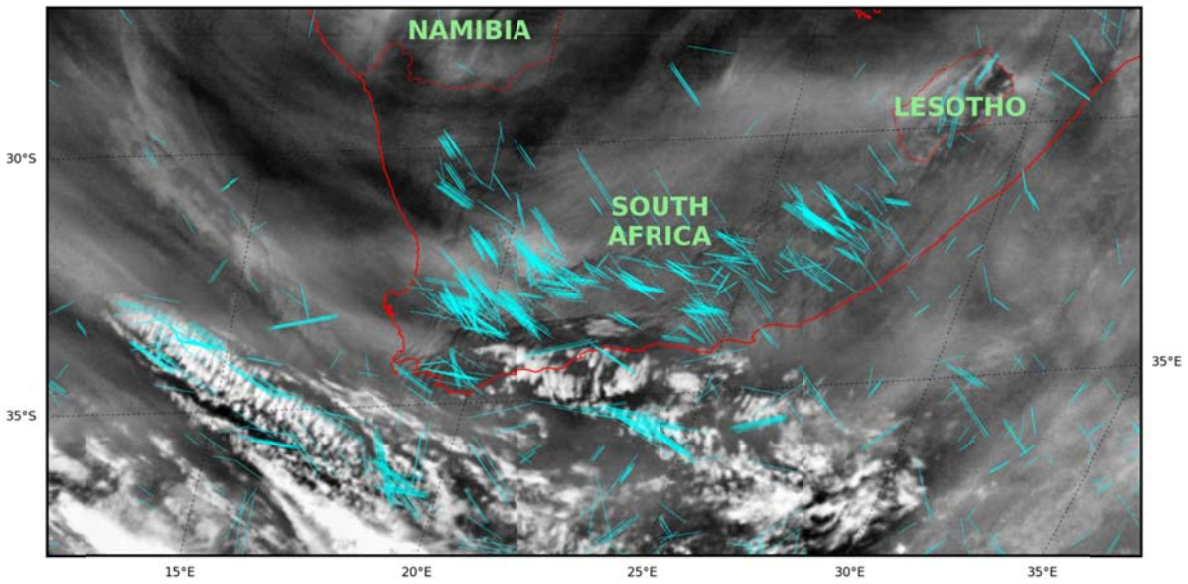

Figure 8: *Same as* ***Figure 6*** *but the detection algorithm being less restrictive on the minimum accepted signal.*

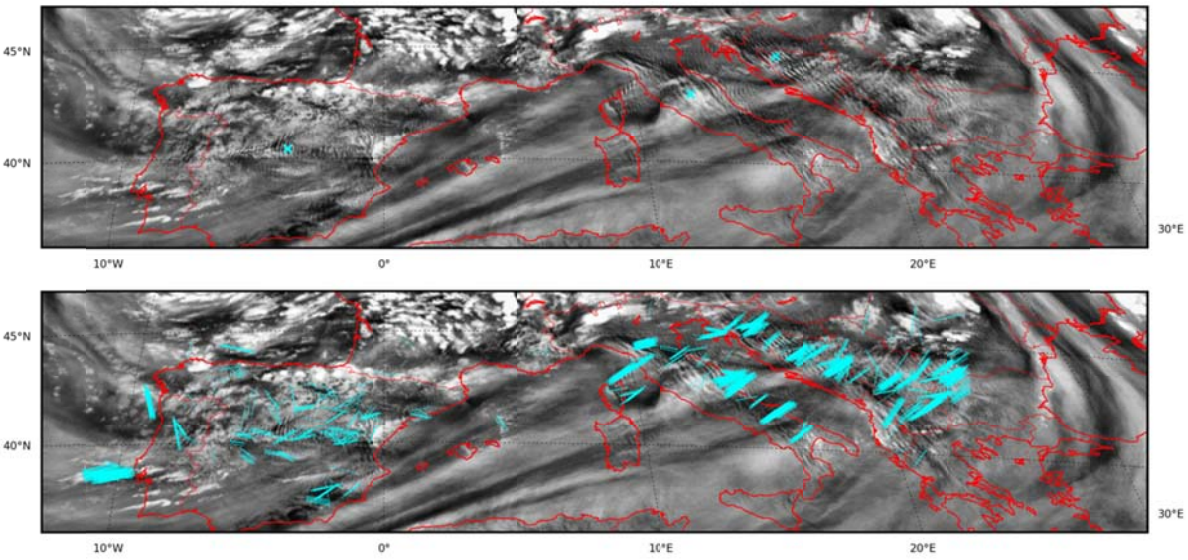

Figure 9: *Upper panel: A European portion of the WV7.3 image of* ***Figure 3****. Cyan crosses mark gravity wave regions deserving particular attention. Lower panel: Same image, with superimposed cyan lines showing the results of the grating detection with the "operational" parameter setting of v2017.*

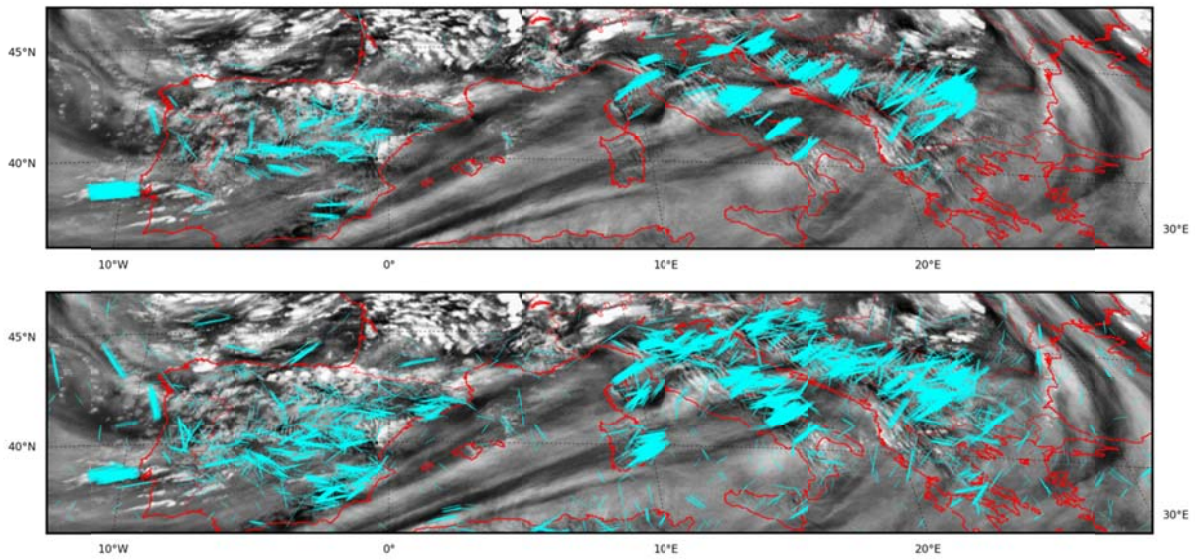

Figure 10: *As* ***Figure 9****, but the superimposed results are from runs with twofold number of angles (upper panel) and looser restriction (*ΔT*=0.1 K) on minimum signal (lower panel).*

2.3.1.2 Europe

The analysis over Europe captures the numerous fields of ripples generally very well (**Figure 9**). However, there are certain regions where it is somewhat surprising that they are not covered over their whole extension though the signatures are quite clear in the images. These regions (in central Spain, central Italy and Bosnia-Herzegovina) are indicated by crosses in **Figure 9**. The same experiments as in the South African case were carried out in order to see whether we can get a more complete detection. Interestingly, this time, increasing the number of inspected angles had more positive impact than the lowering of the temperature fluctuation threshold, at least in the three mentioned "problem areas" and with respect to the additional signals incurred in areas without actual ripples[2] (still, the difference in the signal density is again so pronounced that the occasional false alarms incurred through relaxing the requirement on the signal strength will not penetrate through to the final product). However, by virtue of numerous signals suddenly occurring near eastern Sardinia in **Figure 10**, lower panel, we gained one clear confirmation also in this part of the world that the ΔT threshold was set too strict in v2017.

2.3.1.3 Botswana (plus a closer look at Spain)

Figure 11 shows the vigorous response of the grating search over Botswana, where the appearance in the WV suggests convective origin (if one considers the diurnal variation in a loop, there can in fact be no doubt about it). The regular arrangement of the convective clouds has the basic features of a grating pattern yet something difficult to grasp still tells the human observer that this is somehow different from the ripples seen over South Africa and Europe. Detecting this "somehow more cumuliform appearance" (some authors used the term "string of pearls") can certainly not be taken on board in the current algorithm by tuning a parameter (because one has to concede that the algorithm does what it is designed for: there are parallel stripes and it detects them), but would require a new algorithmic component. The intriguing conclusion from

[2] Nevertheless, trading off the value of such additional signals for the final product against the additional computational effort, the final decision was to deliver v2018 with the original setting of eight tested orientations.

consulting relevant literature is, however, that filtering these signals should perhaps not be attempted at all. There is evidence (e.g. Lane and Zhang (2011), Melfi and Palm (2012)) that such regular arrangements of convective clouds can have their root cause in gravity waves, so the gravity wave diagnosis in **Figure 11** might well be correct.

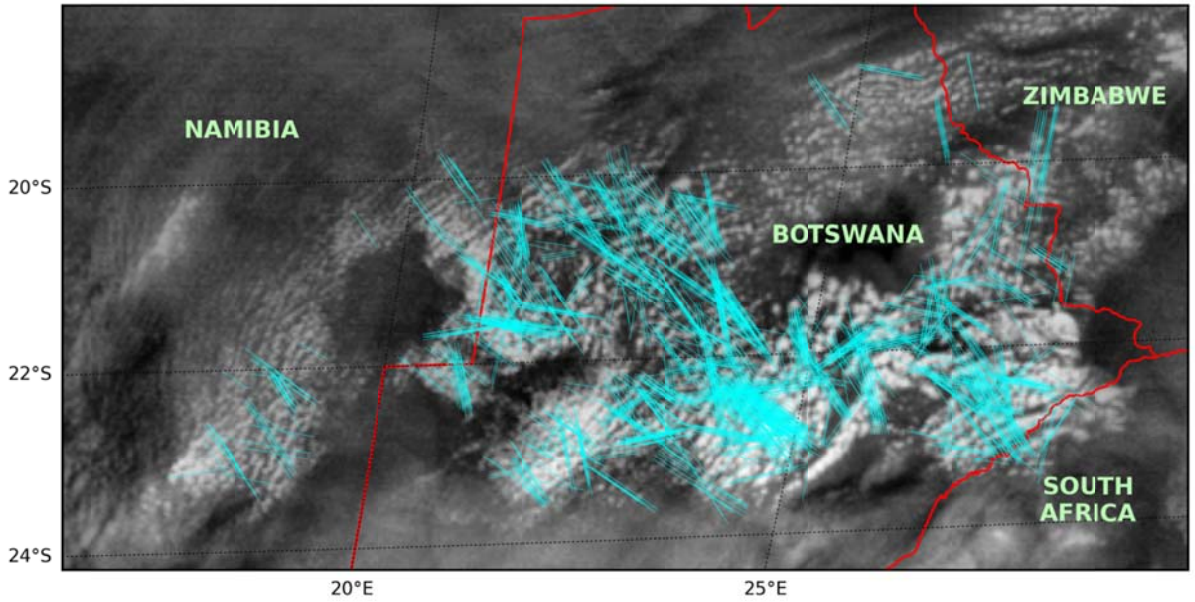

Figure 11: *A southern African portion of the WV7.3 image of* ***Figure 4****. The superimposed cyan lines are those along which the detection algorithm found a grating pattern.*

On the other hand, linear structures may in fact originate from other mechanisms of atmospheric dynamics (Young *et al.*, 2002), and to distinguish between those candidates is certainly not straightforward, probably even impossible, from the Meteosat images alone. Thus, it basically becomes a question of product design whether one retains the hints on regularity (once they are eliminated from the objective analysis, it is an arduous task get them back subjectively!) and consults supplementary material separately or integrates it to make a decision about the root cause inside the objective algorithm.

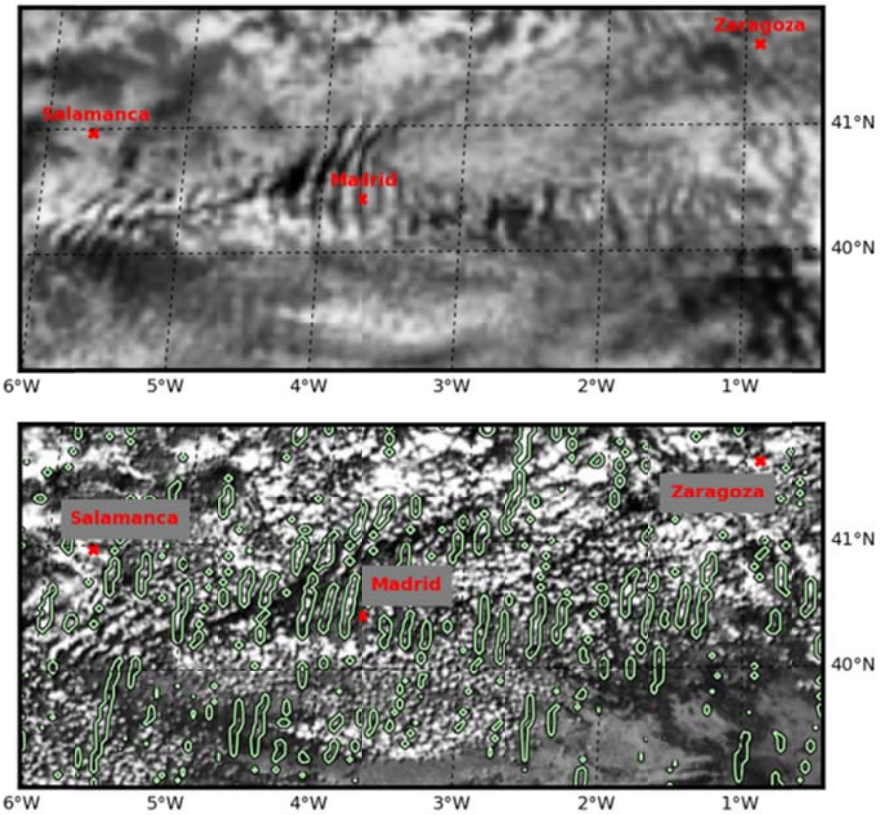

Figure 12: *Upper panel: A zoomed portion of the WV7.3 image of* ***Figure 4*** *(over Spain). Lower panel: Simultaneously recorded Meteosat-10 high-resolution visible imagery. The -1.5-units isoline of the Gabor filter field with λ=4 pixels, Θ=15π/16 is superimposed in order to establish the connection between the ripples seen in the WV image and the structures shown in this HRVIS image.*

Interestingly, the caution against filtering "strings of pearls" is supported by another portion of the SEVIRI imagery taken on 29 June 2017, 1400 UTC. **Figure 12** shows both the WV 7.3 µm image and the high-resolution visible (HRVIS) image over a part of Spain. The HRVIS channel (with threefold spatial resolution) shows convective cloud systems with a similar visual appearance as seen in the WV image over Botswana, though admittedly the organization into lines is not as distinguished. The convection at this moment apparently was not developed strongly enough to make the "string of pearl" pattern penetrate through to the layer covered by the WV 7.3 µm image, so in this image one enjoys an undisturbed view of gravity wave ripples. Though the two phenomena convection and gravity wave are divided between the two channels at 1400 UTC, a linkage through three-dimensional atmospheric dynamics still may be inferred. The superposition of a suitable Gabor response field of the WV imagery over the HRVIS image in **Figure 12** suggests a connection between the waves and the cloudy to cloud free alternation, most clearly west of Madrid. **Figure 13** gives a glimpse on the temporal evolution over the Iberian peninsula where the atmosphere had been prone to gravity wave formation all day long. At 0000 UTC, there are ripples all over the place in the WV 7.3 µm image, and any convective background of the patterns can be ruled out after inspecting the infrared 10.8 µm image (quite the contrary: the gravity waves in some places shape the stratiform cloud deck). Gravity waves came first, and when convection developed later that day, it was at least partly reinforced and shaped by those waves. So, if responses to the resulting regularity were obtained from a tailored grating detection

algorithm applied to an afternoon HRVIS image, they would actually point to a present gravity wave, backing the view that dismissing string-of-pearls gratings is a disputable approach.

Altogether, it is suggested to accept the convection line signals in the final product[3]. A standard satellite loop should easily reveal the *simultaneous* onset of convection and grating reports. Thus, the affected areas are quickly spotted in meteorological routine as ones where the risk of an error when attaching the "gravity wave" label is higher[4].

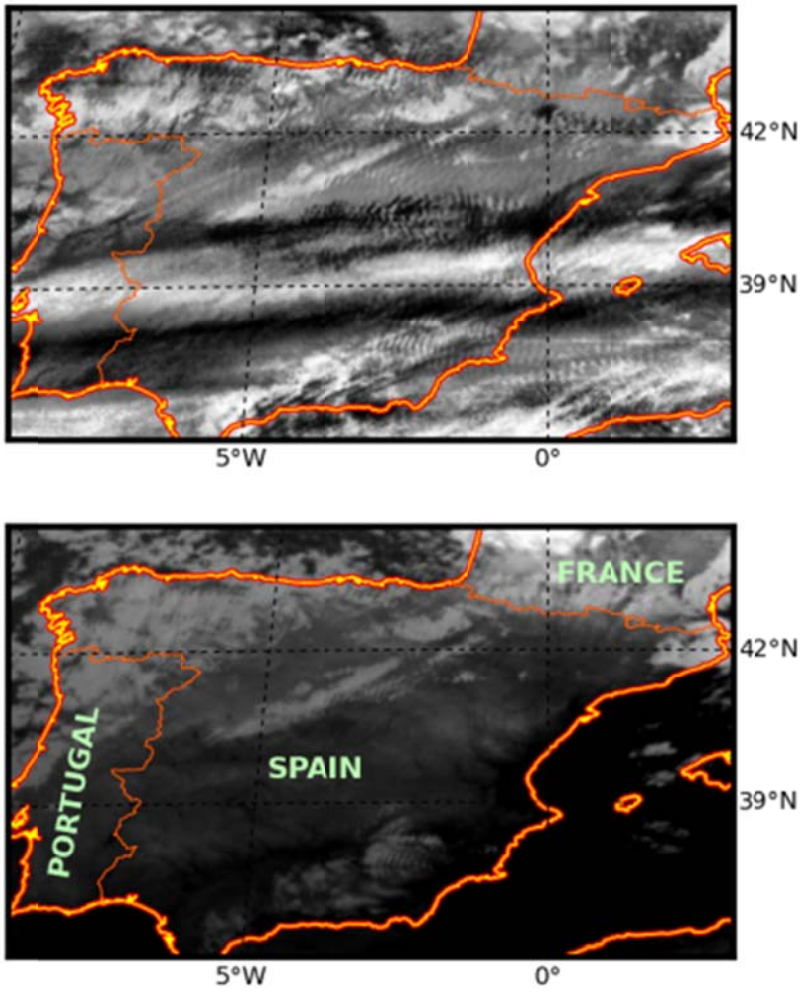

Figure 13: *Upper panel: Meteosat-10 7.3µm water vapour image recorded over the Iberian peninsula on 29 June 2017, 0000 UTC, showing widespread gravity wave ripple signatures in the northern and eastern sectors. Lower panel: The simultaneously recorded Meteosat-10 10.8 µm infrared image.*

[3] And it is probably safe to claim that the WV channels are those least affected by the other phenomena producing linear structures listed in Young *et al.* (2002) (which even has "boundary layer" in its sub-title)

[4] Ironically, the meteorologist may still have been alerted about a region critical for aviation, though for the wrong reason.

2.3.2 29 June 2017, 1630 UTC

As no distinct new features were observed at other times of the day, presenting more cases in such detail as in section 2.3.1 does not seem worthwhile. However, it could be of interest to briefly address the difference in ASII-GW analyses from Meteosat-8 (41.5°E) and Meteosat-10 (0°), respectively. Starting with the northern hemisphere (**Figure 14**), one can see that the situation over Europe has not changed much in the 2.5 hours between **Figure 3** and **Figure 14**: many signals over Spain, Italy and the Balkans. Actually, for the latter two, both satellites detect the widespread presence of the waves, whereas Spain seems to be too far on the limb of the disc and the geometric distortion is already too strong to warrant identification of the phenomenon (we are in any case already quite courageous by trying to identify waves on the scale of a few kilometres in the ordinary SEVIRI channels, so problems towards the edge of the disc, where patterns become increasingly blurred, come as no surprise). The different strengths of the signals over Northwest Africa might be explained similarly (actually, it is convection and resembles the Botswana situation discussed above). For the Southern Hemisphere, both satellites indicate the waves over South Africa (but as in **Figure 6**, the extension is underestimated). Also in the ocean around Antarctica, the algorithm qualitatively responds to the same patterns for both satellites, despite of partly extreme viewing angles. As a side-remark, the signals over Botswana have now almost vanished: the convection has meanwhile developed so far that almost everything in this area is cloud-covered and the stripy patterns are gone.

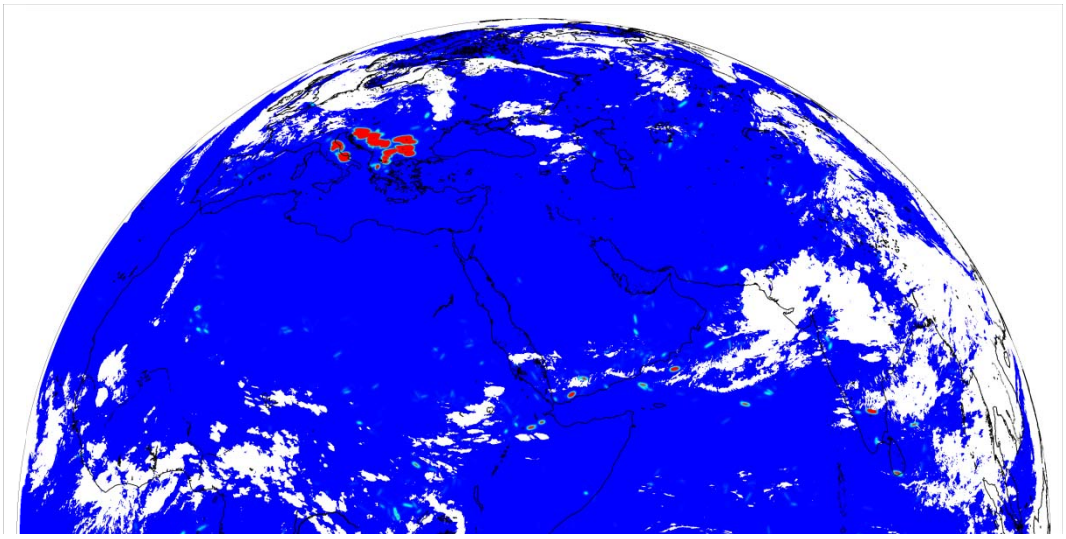

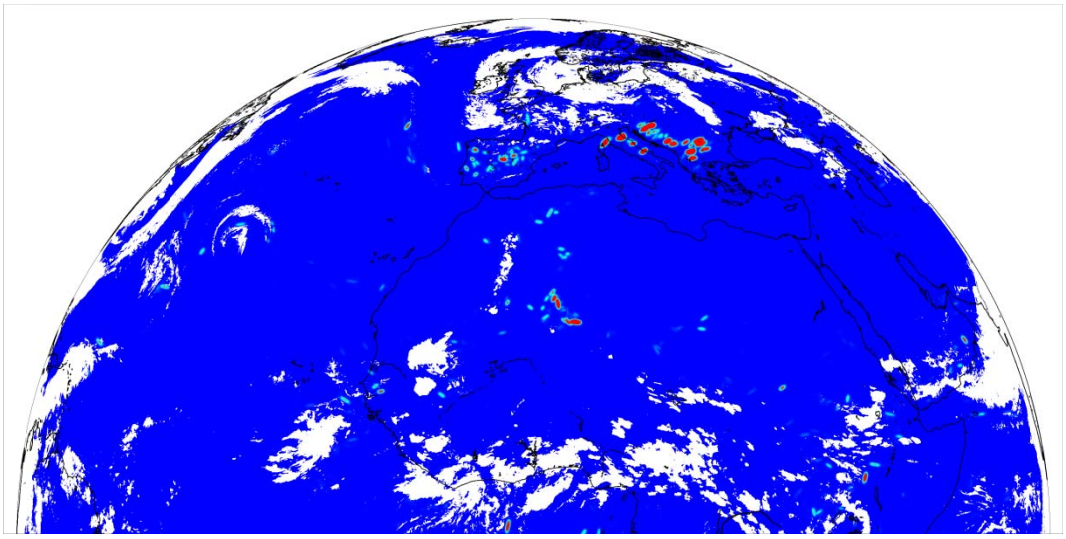

Figure 14: *Case of 29 June 2017, 1630 UTC, Northern hemisphere. Upper panel: The ASII-NG probability-of-gravity-wave product based on the MSG-1 WV7.3 image. Lower panel: The ASII-NG probability-of-gravity-wave product based on the MSG-3 WV7.3 image. Colour table as in* ***Figure 2****: areas with 0% probability in dark blue; 100% probability signalled in red; the areas masked by the temperature threshold to avoid random signals in thick clouds are shown in white.*

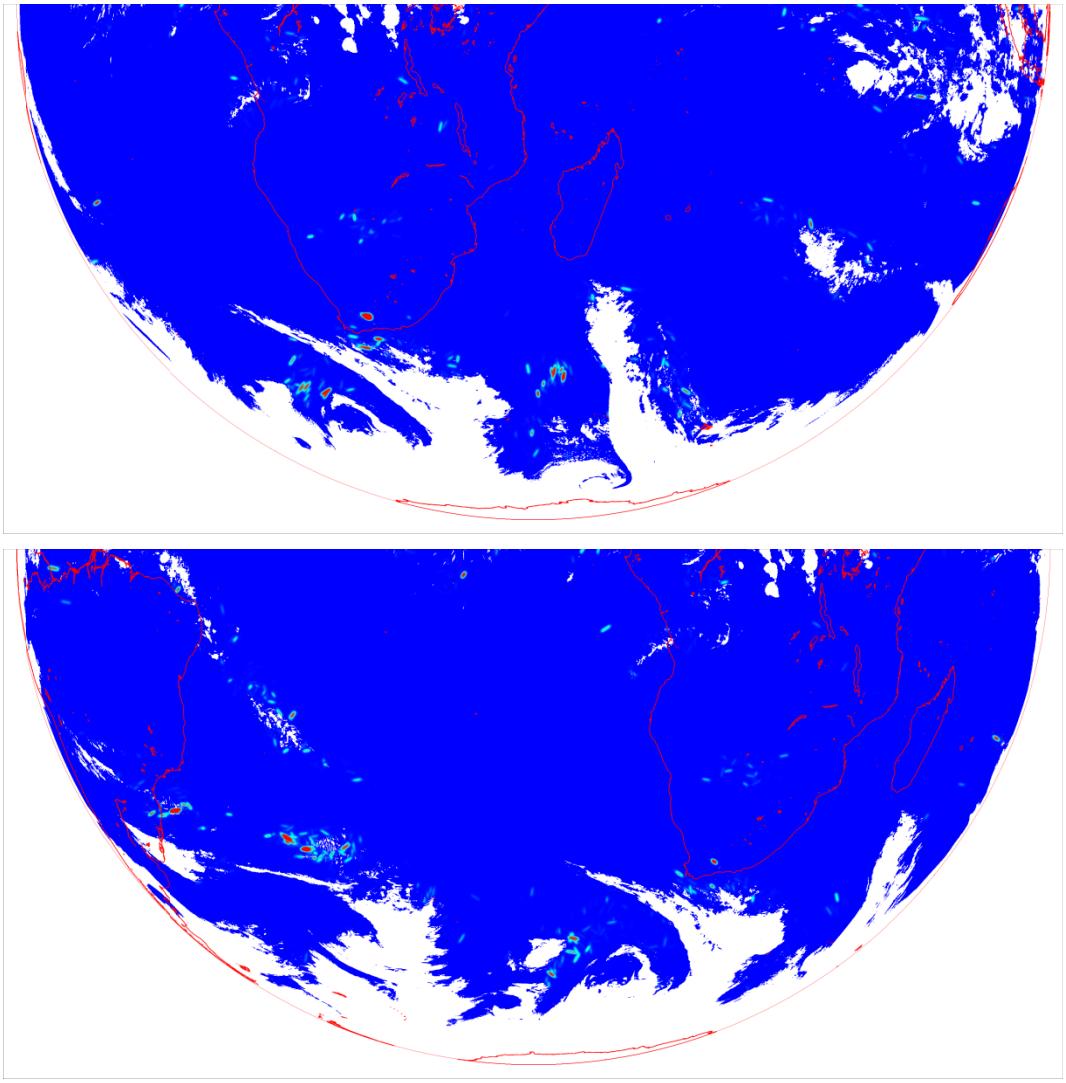

Figure 15: *Same as* ***Figure 14****, but for the southern hemisphere.*

2.4 CONCLUSIONS

The ASII-NG gravity wave detection directs the meteorologist in a time-saving manner to those areas where gravity waves can be seen in WV7.3. False detections are kept at very low rates, and their occurrence is understandable from the construction of the algorithm and the optical appearance of the affected meteorological phenomena. It is fortunate that these phenomena can be quickly identified as "something else" through visual inspection. This, on the other hand, is also motivation to understand what it is that makes the human observer quickly obtain this distinction, and to possibly clear the product also from these signals in future releases. Any progress in this area should also bring us closer to applicability of the technique to other channels, where the

false-alarm rate is currently too high, but where gravity waves are sometimes indicated that are not visible in the currently used WV7.3 channel. Currently, we are inclined to consider the signals from regularly arranged convection as in **Figure 11** as valuable, i.e. to make no attempts to filter them, which makes the work on cases of incorrectly flagged areas of marine stratocumulus top priority.

2.5 LAST-MINUTE UPDATES

At the moment of freezing the PGE for release NWC/GEO v2018, we have settled on a ΔT of 0.17 K. Therefore, the number of hits lies somewhere between the initial version with 0.4 K and the experimental version with 0.1 K used when producing the main body of the validation report. The general conclusions are not affected by this fixing, of course. For the sake of completeness, ***Figure 16***–***Figure 18*** revisit the three regions of South Africa, Europe and Botswana and show the outlook of the final product (i.e. after transforming the hits into a signal density map which then in turn is transformed via a logistic relation into a 0-100% probability map) with the settings chosen for the delivered code.

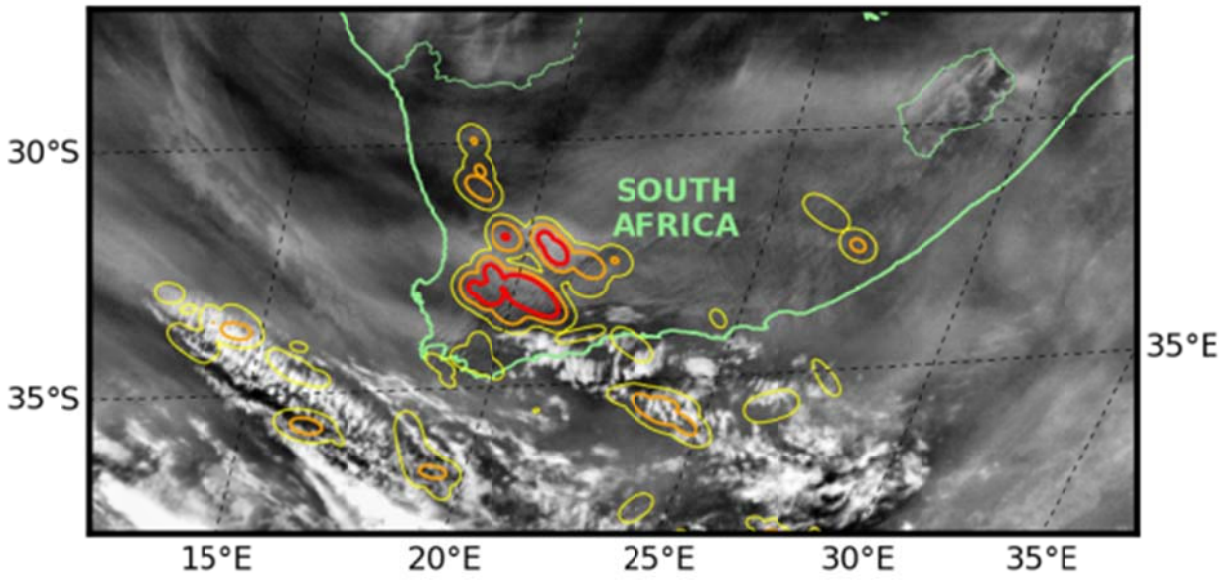

Figure 16: *The WV7.3 image of 29 June 2017, 1400 UTC, South Africa and surrounding ocean, superimposed by the 1, 50 and 99% isolines of probability of gravity-wave occurrence, as indicated by the ASII-GW product, v2018.*

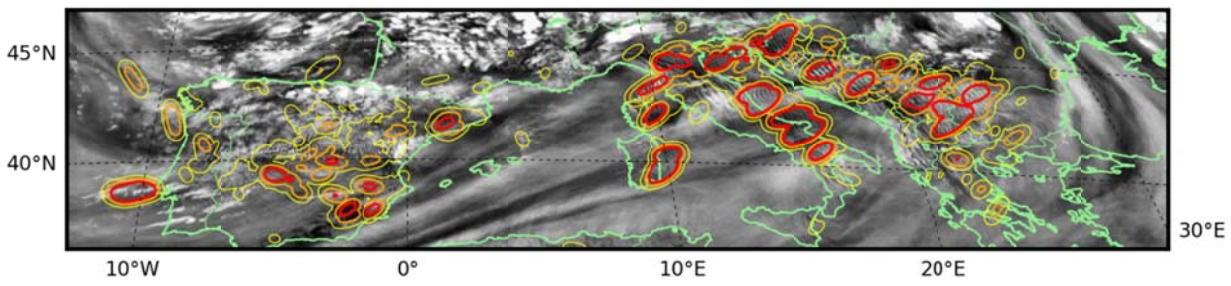

Figure 17: *The WV7.3 image of 29 June 2017, 1400 UTC, over Mediterranean Europe, superimposed by the 1, 50 and 99% isolines of probability of gravity-wave occurrence, as indicated by the ASII-GW product, v2018.*

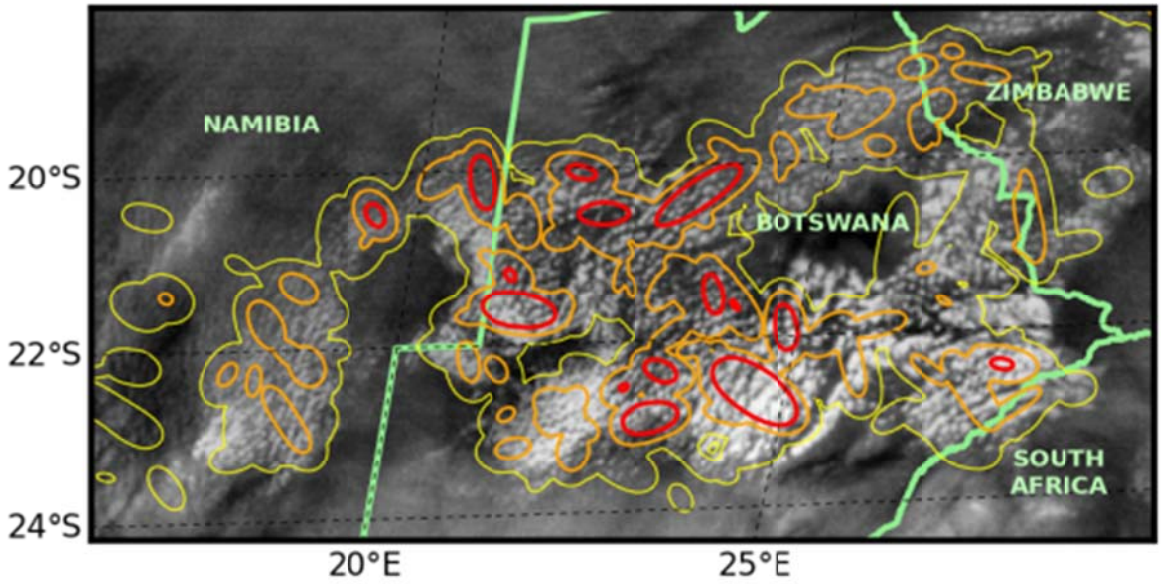

Figure 18: *The WV7.3 image of 29 June 2017, 1400 UTC, over Botswana, superimposed by the 1, 50 and 99% isolines of probability of gravity-wave occurrence, as indicated by the ASII-GW product, v2018.*

Concerning the exercise undertaken in 2.3.2, we have meanwhile recognized in the South African case that differences between Meteosat-8 and Meteosat-10 analyses (obtained with an experimental version of the algorithm that addresses some of the mentioned open issues) were not attributable to a shortcoming of one of the analyses. It rather had to be acknowledged that the Meteosat-8 analysis simply reflected the much more distinct picture this satellite provided about the ripples in some parts. The situation of Meteosat sensing water vapour in the atmosphere is indeed different from viewing a metal grating as a human and recognizing it from all angles, which limits transferability of concepts from one process to the other. First, the satellite at the 7.3 µm wavelength receives radiation from a relatively thick layer, not the surface of an object. The outcome therefore depends on the three-dimensional distribution of moisture, viewed slantwise from space. And unlike a human, the satellite cannot adapt its lens to the details wished to be seen. It always has the same spatial resolution, the same pixels at the same position. The phenomenon of gravity waves often has a scale that is comparable to the pixel resolution, so the positioning of pixels can indeed be relevant to the recognisability of a wave. In a nutshell, there are too many factors outside of the algorithm which may also serve to explain different outcomes for Meteosat-8 and Meteosat-10, respectively. We therefore believe that (automatic) inter-satellite ASII-GW comparison is not a viable option for future validation efforts, and comparison with subjective analysis of scenes still remains the method-of-choice, at least for application to the WV 7.3 µm imagery (for a potential HRVIS application, this might be a different story as it is rather the surface that is pictured and the spatial resolution is higher).

2.6 REFERENCED SCIENTIFIC PUBLICATIONS

Brown, B.G., and G.S. Young (2000): Verification of icing and turbulence forecasts: Why some verification statistics can't be computed using PIREPS. 9th Conference on Aviation, Range, and Aerospace Meteorology, Orlando, FL, 11-15 September 2000, 393-398.

Fritts, D.C., and M.J. Alexander (2003): Gravity wave dynamics and effects in the middle atmosphere. *Rev. Geophys.,* **41,** *1003, doi:10.1029/2001RG000106.*

Jann, A. (2017): Detection of gravity waves in Meteosat imagery by grating cell operators. *Eur. J. Remote Sens.*, **50,** 509-516. http://dx.doi.org/10.1080/22797254.2017.1367629.

Kruizinga, P., and N. Petkov (1995): A computational model of periodic-pattern-selective cells. In J. Mira & F. Sandoval (Eds.), *Proc. IWANN'95, Lecture Notes in Computer Science 930* (pp. 90–99). Berlin: Springer.

Kruizinga, P., and N. Petkov (1999): Nonlinear operator for oriented texture. *IEEE Trans. Image Proc.,* **8,** 1395-1407. doi: 10.1109/83.791965.

Lane, T.P., and F. Zhang (2011): Coupling between gravity waves and tropical convection at mesoscales. *J. Atmos. Sci.*, **68**, 2582-2598.

Melfi S.H., and S.P. Palm (2012): Estimating the orientation and spacing of midlatitude linear convective boundary layer features: Cloud streets. *J. Atmos. Sci.*, **69**, 352-364.

Petkov, N., and P. Kruizinga (1997): Computational models of visual neurons specialised in the detection of periodic and aperiodic oriented visual stimuli: bar and grating cells. *Biol. Cybern.*, **76,** 83-96.

Sharman, R., and T. Lane (Eds.) (2016): *Aviation turbulence: Processes, detection, prediction.* Springer International Switzerland. doi: 10.1007/978-3-319-23630-8_23

Young, G.S., D.A.R. Kristovich, M.R. Hjelmfelt, and R.C. Foster (2002): Rolls, streets, waves, and more. A review of quasi-two-dimensional structures in the atmospheric boundary layer. *Bull. Amer. Meteor. Soc.*, **83,** 997–1001, https://doi.org/10.1175/1520-0477(2002)083<0997:RSWAMA>2.3.CO;2 [Extended version designated "Supplement", pp. ES54-ES69, available on-line at https://journals.ametsoc.org/doi/pdf/10.1175/BAMS-83-7-Young (accessed February 2018)]

3. VALIDATION OF THE ASII-NG TROPOPAUSE FOLD PRODUCT, V2.0

As described in the ASII-NG ATBD [RD.3], this product suite shall comprise modules relevant for aviation meteorology, through objective detection of patterns generally considered as indicative of (clear-air) turbulence. Though the significance of features like tropopause folds is commonly acknowledged among aviation meteorologists for being indicative to regions related to frequent occurrence of turbulence, this is nevertheless an indirect relationship. The turbulence experienced by aircrafts passing through these zones has its root cause in wind shear within or in the vicinity of jet streaks (characterized by wind speeds higher than 30m/s within the jet) which in turn are closely connected to the phenomenon of tropopause folds.

For every MSG/SEVIRI pixel, the ASII-TF output provides a probability (0-100%) of the presence of a tropopause fold at that location.

The validation of turbulence detection algorithms has been undertaken in the past by using PIREPs as a confirmation for atmospheric turbulence (Ellrod and Knapp, 1992, Vieira, 2005, Wimmers and Feltz, 2006). Unfortunately, while able to provide such a confirmation, the absence of a PIREP does not mean the absence of turbulence. Though providing this incomplete picture of atmospheric turbulence, PIREPs have been used in the past to tune turbulence detection algorithms (Sharman et al., 2006).

This validation report of the ASII-TF product consists of three parts. First the ASII-TF output will be compared to turbulence reports (PIREPs) from passenger airplanes; second, the ASII-TF output will be compared to the position of tropopause folds calculated from IASI level-2 vertical sounding data from MetOp satellites, and third the performance of the ASII-TF output will be assessed for a day with numerous turbulence warnings.

3.1 VALIDATION OF THE ASII-TF PRODUCT AGAINST PIREPS

The Pilot Reports (PIREP) used to validate the ASII-TF product were issued over Europe in the time period of **16 April to 20 June 2018**; most of them in and around the Austrian airspace. All 196 PIREPs used in this validation campaign were located within the region covered by the ASII-TF product (see **Figure 19**).

Dissimilar types of aircrafts sense turbulence differently, hence the PIREPs were split up by aircraft types. The evaluated reports stem from pilots of larger civil airplanes only, denominated either as "heavy" or "medium" in the PIREP or by their full denomination (e.g. "A320"). Reports from small aircrafts were not taken into account because they mainly cruise in levels below the tropopause folds and are much too sensitive to vertical accelerations. The region covered by the ASII-TF product in this investigation is Central and Western Europe (see **Figure 19**); all PIREPs used for validation were located within this region.

By analyzing the synoptic situation at the geographical positions for which the turbulence warnings (PIREPs) were issued, three main sources for turbulence could be identified from satellite and NWP data:

- Convection
- Lee waves (gravity waves)
- Wind shear (directional and velocity shear)

Ongoing convective activity was mainly recognized from satellite image and radar data while the occurrence of lee waves was observed both in model (wind field) and satellite data. Wind shear was calculated on model surfaces.

Among the above listed turbulence sources, only wind shear is related to tropopause folds; therefore, validation will focus on the ability of the ASII-TF product to forecast turbulence related to strong upper-level wind changes in direction and speed. Strong vertical wind shear, in most cases, is caused by jet streaks at the 300 hPa level and above. Jet streaks on their side are closely connected to frontal zones (i.e. horizontal temperature gradients). The validation will hence investigate the relationship between high wind shear as a cause of turbulence and the results of the ASII tropopause fold detection product.

Figure 20 shows an example of pilot reports from two different locations over Spain plotted on the output of the ASII-TF software. The time slot of the ASII-TF product is chosen to be nearest to the date of issue of the PIREP.

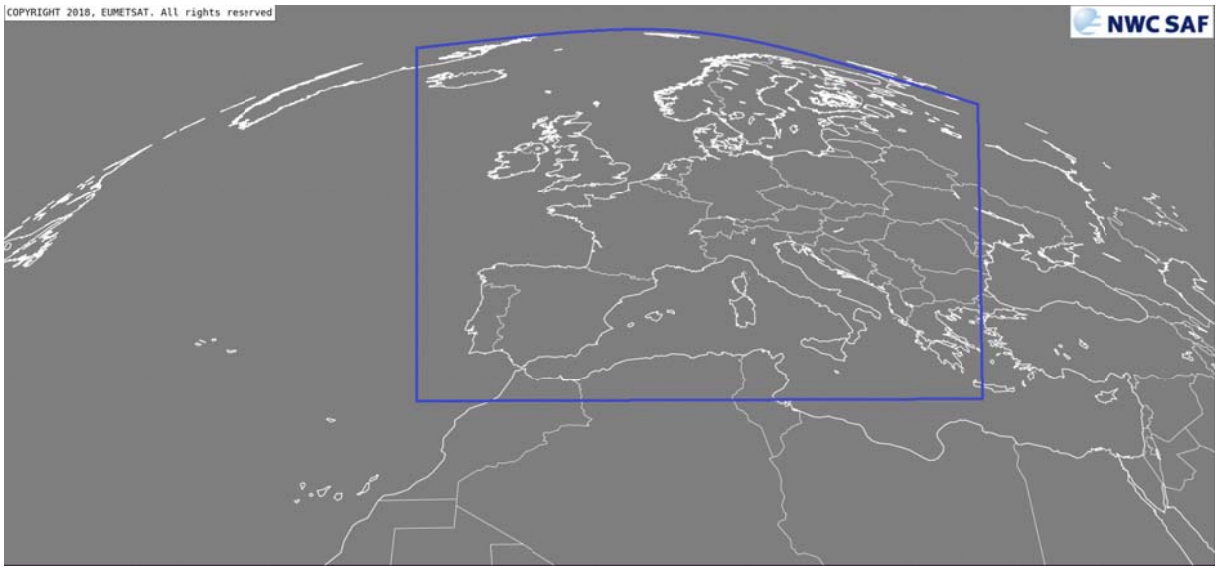

Figure 19: *The blue line delimits the area of the ASII-TF analysis used in this evaluation.*

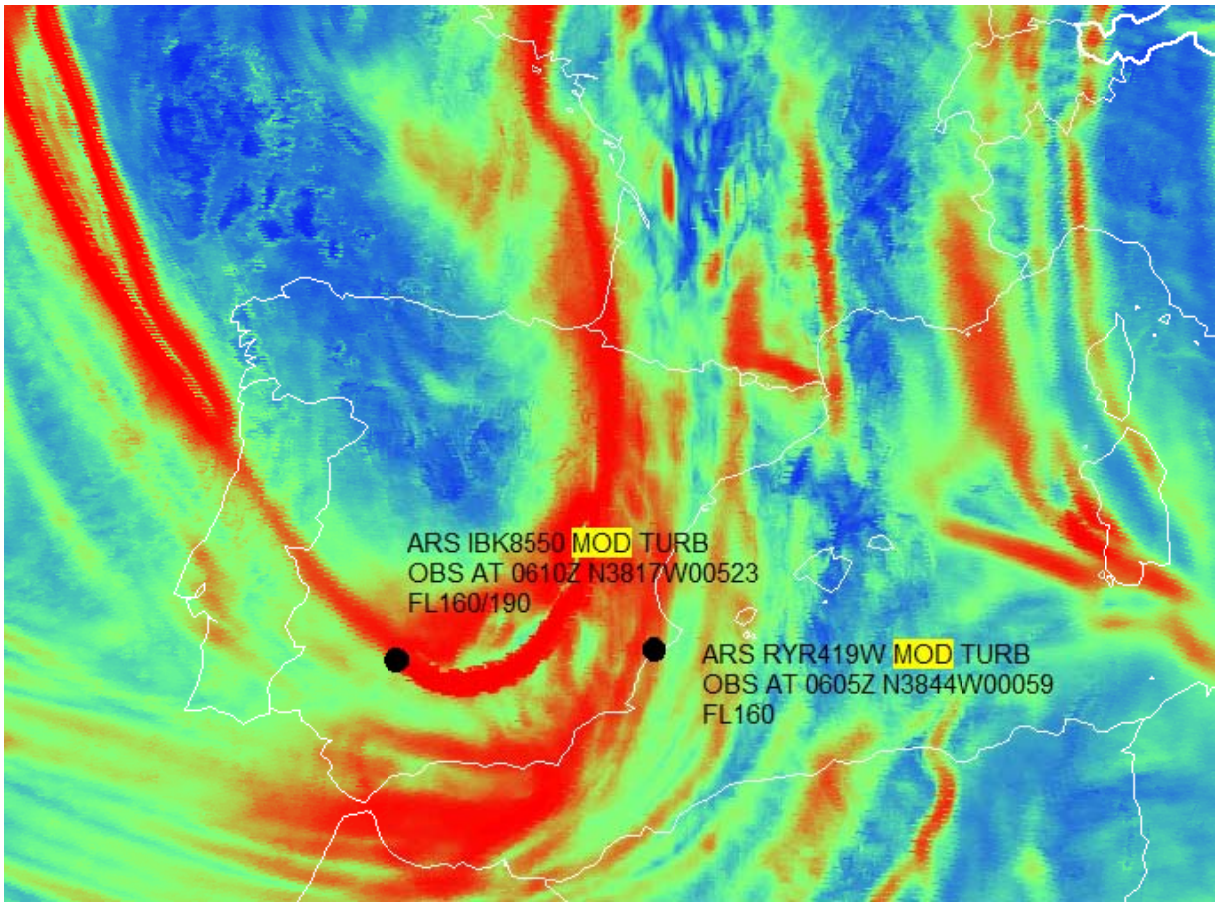

Figure 20: *Example of Pilot Reports (black dots) and associated text lines of the Pilot Report located on the ASII-TF product. Date: 29 April 2018, 06:00 UTC.*

A total of **196** turbulence reports were evaluated in the period 16 April-20 June 2018. Four categories of turbulence intensities were considered: light/moderate, moderate, moderate/severe, and severe. The results of the ASII-TF product were divided into 3 categories: high probability for being at a tropopause folding (67-100%), medium probability (34-66%) and low probability (0-33%). **Table 3** summarizes all turbulence reports without taking into account the source of turbulence.

ASII-TF [%]	total	LGT/MOD	MOD	MOD/SEV	SEV
67-100	48	7	32	3	6
34-66	100	22	66	3	9
0-33	48	7	34	2	5

Table 3: *Number of all turbulence reports as a function of their intensity and their assigned ASII-TF probability (LGT: light, MOD: moderate and SEV: severe).*

Most aircraft pilots report turbulence caused by wind shear at flight levels (FL) from above the jet axis, i.e. the region with the highest wind speed (48 PIREPs came from FLs above the jet axis, and 20 reports came from below this region). The reported flight levels ranged from FL80 to FL390 during the whole period. This corresponds to pressure levels between 750 and 200 hPa

approximately. The vast majority of cases were issued by "en route" aircrafts at high altitudes (FL360-380).

When focusing only on those turbulence reports related to strong wind shear (i.e. directional and velocity shear), the number of reported incidents reduces to 131 (see **Table 4**).

ASII-TF [%]	total	LGT/MOD	MOD	MOD/SEV	SEV
67-100	40	6	26	2	6
34-66	74	17	51	2	4
0-33	17	2	14	1	0

Table 4: *Number of turbulence reports caused by strong vertical wind shear as a function of their intensity and their assigned ASII-TF probability (LGT: light, MOD: moderate and SEV: severe).*

Comparison of **Table 3** with **Table 4** shows that most MOD/SEV and SEV turbulence reports falling in the category 67-100% probability for an ASII tropopause folding are caused by strong wind shear and not by convection or orographic waves (orange boxes). When summing up all turbulence reports in **Table 4** related to strong wind shear (i.e. directional and velocity shear) with an ASII-TF probability higher than 34%, more than 87% of the turbulence reports fall into this category. In other words, the lowest ASII-TF category (0-33%) contains only about 13% of the turbulence reports related to strong wind shear and none of them is severe (yellow box). We also see in both tables that the ASII-TF category 34-66% contains the largest number of turbulence reports (green boxes) and in **Table 4** a clear shift from moderate to severe turbulence when the ASII-TF probability increases.

When further comparing **Table 3** with **Table 4**, validation shows that the percentage of turbulence reports falling into the highest ASII-TF category (67-100%) increases from 24.5% to 30.5% when only wind (shear) related incidents are considered. When all ASII-TF probabilities above 34% are considered, the hit rate increases from 75.5% to 87%. The number of misses (ASII-TF category 0-33%) reduces from around 24.5% to 13% when only wind (shear) related incidents are considered (i.e. lee wave and convection related turbulence is excluded).

These results show a strong connection between tropopause folds and turbulence caused by wind shear and strong upper level winds.

Table 4 shows that most PIREPs reporting turbulence come from areas showing a medium probability for a tropopause folding (74 reports, green box). These areas, also shown in green in **Figure 21**, often mark a transition zone to red areas (i.e. high tropopause folding probability). This cumulation could be explained by the assumption that pilots issue a turbulence warning when they enter a region of turbulence. But this assumption is hard to prove, as PIREPs do not describe the direction of the flight.

Most of the turbulence reports showing a low ASII-TF probability origin from convection. As can be seen in **Figure 22**, convective cells are depicted by uniformly blue patches showing low ASII-TF probability values.

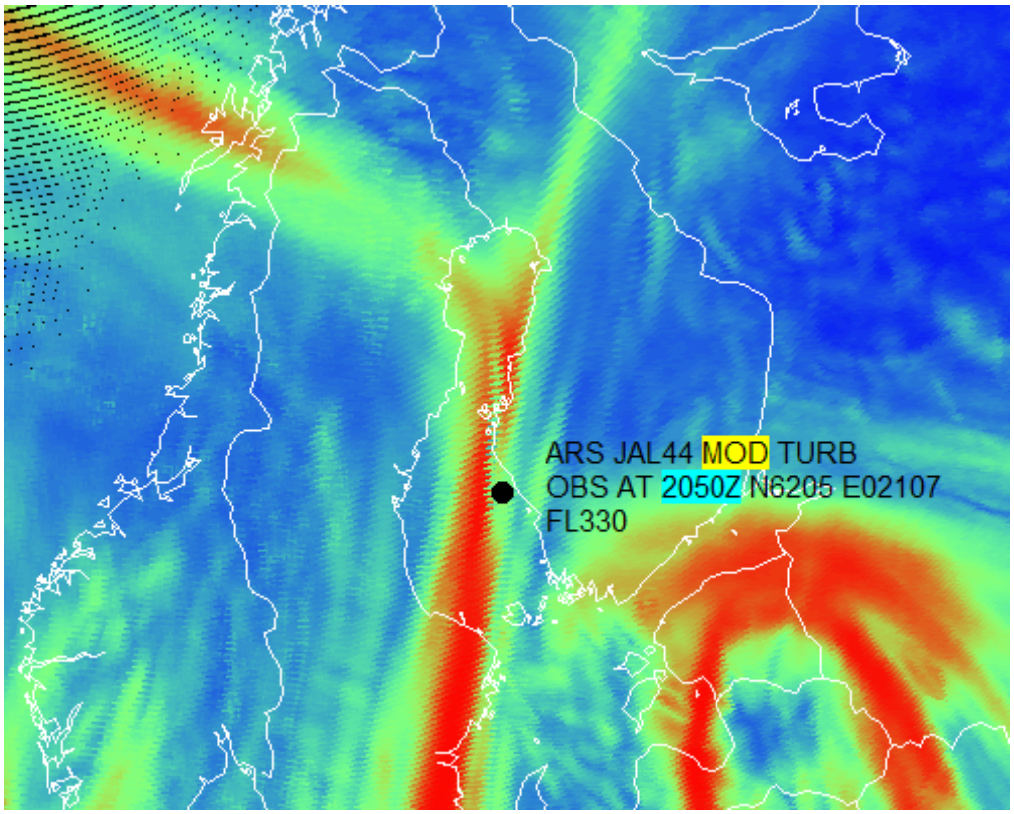

Figure 21: *ASII-TF product from 24 June 2018 at 20:45 UTC. The indicated PIREP position (black dot) lies in the green area of medium probability values and near to the red zone of high probability values of being at a tropopause fold.*

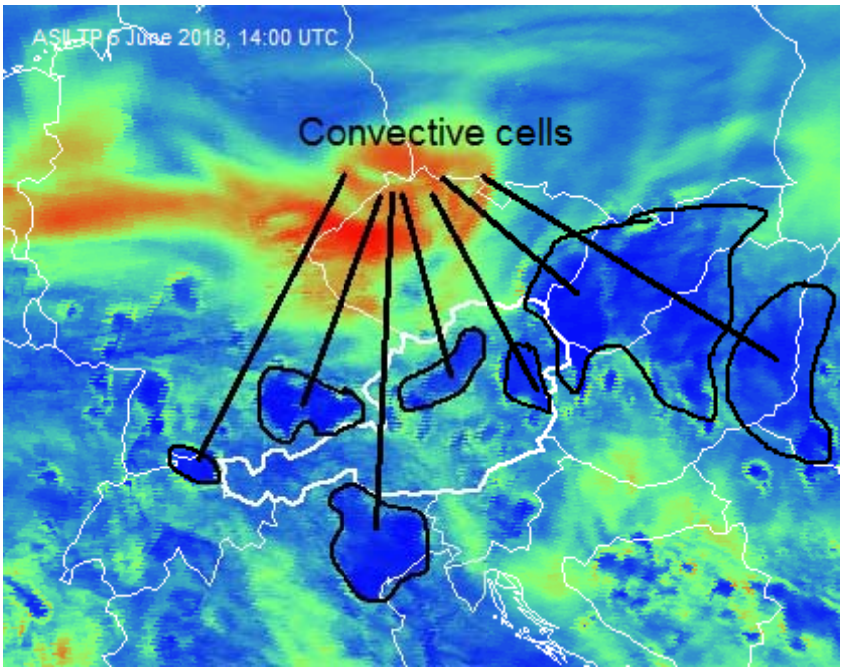

Figure 22: *ASII-TF product from 6 June 2018 at 14:00 UTC. Convective cells are depicted with a low probability for being located near a tropopause fold (red: high probability, green: medium probability and blue: low probability).*

An increase of turbulence reports related to convection was noticed on some days (e.g. 11 – 13 June 2018). Apart from days with prevailing convective activity, the number of turbulence reports related to wind shear remained constant in the observed period.

When we take the same sample as in **Table 4** (i.e. exclude pilot reports related to convection or gravity waves), the remaining turbulence reports can be divided into 3 categories[5]:

1. Wind shear related to wind speed differences in different levels (vertical velocity shear)
2. Wind shear due to strong curvature of the air stream at a given pressure level (curvature shear)
3. Wind shear resulting from diverging wind directions in different levels (directional shear)

The latter two categories both represent directional shear either on the same level (green box in table 3) or in between different levels (blue box).

ASII-TF [%]	Total number	1. Vertical velocity shear between different levels	2. Curvature shear in the same level	3. Directional shear between different levels
67-100	40	40	0	0
34-66	74	63	10	1
0-33	17	8	4	5

Table 5: *Number of turbulence reports associated with strong curvature of the wind trajectory (green), by vertical wind shear resulting from velocity (orange) and by directional shear (blue) as a function of their assigned ASII-TF probability.*

Table 5 shows that most turbulence warnings are issued because of velocity shear (orange box: 111 out of 131 reports). It also shows that the number of turbulence incidents caused by directional wind shear (vertical and horizontal) is biased towards lower ASII-TF probability values (green and blue box) while the number of incidents caused by vertical velocity shear (orange box) is biased towards higher probabilities.

Velocity shear represents the most frequent source for reported turbulence in PIREPs. However, we find the largest numbers of reports in the middle category of ASII-TF probability values (yellow box) and not in the highest category. A closer look on the geographical location of the turbulence reports in this category shows that 48 of 74 turbulence reports were released in direct vicinity to areas with the highest ASII-TF category [67-100%] (see **Figure 21**), while 26 reports falling into the middle category [34-66%] were not located in the neighborhood of a region with the highest ASII-TF category.

Among these 48 reports located near but not within an ASII-TF maximum, 8 PIREPs locate turbulence on the anticyclonic side of the jet, 9 on the cyclonic side and 31 at the jet axis - a clear cumulation of the turbulence reports at the jet axis but no preference for one of the jet streak flanks.

As an outcome of the validation campaign, it can be stated that jet streaks (i.e. regions with strong wind shear), frequently located near tropopause folds, are the main source of turbulence. The

[5] These three categories were determined from NWP data. A vertical cross section through each PIREP location was calculated.

obtained results show that areas affected by intense vertical and horizontal wind shear in jet regions are much more extended than indicated by the mere position of the tropopause folds. Even though wind speed and shear vorticity are input parameters, the ASII-TF product is tuned towards showing the position of the tropopause folds. In case the user wants to use ASII-TF as turbulence forecasting tool, the position of the jet streak has to be included as an additional criterion to better forecast regions prone to turbulence which often extend beyond the narrow band of the tropopause fold. The same can be stated for directional shear (horizontal as well as vertical) which is also a noteworthy source of turbulence. Curvature and vertical directional shear as potential source of turbulence are not reflected in the ASII-TF product. If the ASII-TF product is intended to be used as a turbulence forecasting tool, curvature and vertical directional shear should be considered as well.

3.2 COMPARING THE ASII-TF OUTPUT AGAINST IASI LEVEL 2 DERIVED TROPOPAUSE FOLDS

For validation purposes, vertical humidity profiles derived from measurements of the IASI instrument onboard MetOp satellites were used to calculate the tropopause height in order to obtain an independent data source. Up to 4 overpasses of the IASI instrument were recorded each day over the ASII-TF domain. The usefulness of the atmospheric water vapor mixing ratio for locating tropopause folds has been described by Robichaud (2006) who showed in his case study of a remarkable tropopause folding over Eastern North America that this parameter is a reliable indicator for tropopause folds at fronts. Moreover, the algorithm used to derive the tropopause height from humidity profiles turned out to be more reliable than from temperature profiles. Here, a fixed threshold of the mixing ratio was chosen ($2*10^{-5}$ kg/kg) for the deduction of the tropopause height from humidity values. Finally, the gradient of the tropopause height was calculated for each grid point of the IASI overpass.

IASI measures in the infrared part of the electromagnetic spectrum at a horizontal resolution of 25 km over a swath width of about 2,200 km. The vertical profiles of the IASI level 2 product used in this evaluation have a vertical resolution of 1 km. Horizontally, IASI provides 30 measurements in each across track scan (i.e. within the 2,200 km swath). Due to the scanning geometry, the horizontal resolution degrades with increasing viewing angle. At each overpass, the IASI instrument covers only a small fraction of the ASII-TF domain. Moreover, its horizontal resolution is coarser than the ASII-TF resolution which is identical to the image data resolution of the SEVIRI instrument.

The comparison between ASII-TF probabilities and IASI level-2 derived tropopause gradients was done in the area of the NWCSAF domain (see **Figure** 1) over a period also covering validation campaign (i.e. 16 April to 20 June 2018). Correlation analysis between ASII-TF probabilities and the IASI derived tropopause gradient shows a clear positive relationship (correlation coefficient ~0.5).

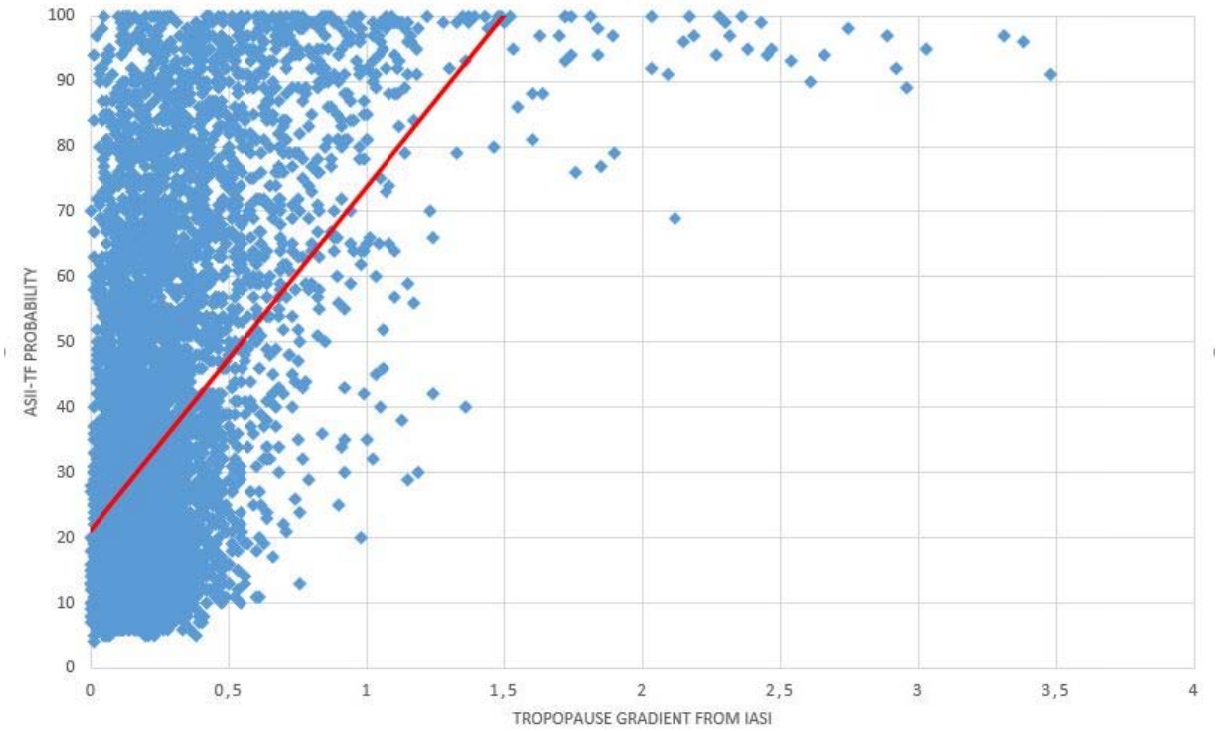

Figure 23: *Scatterplot of IASI level-2 tropopause gradient versus ASII-TF probabilities for 22 March 2018, 09:00 UTC overpass. The red line depicts the linear regression line; the correlation coefficient is 0.52.*

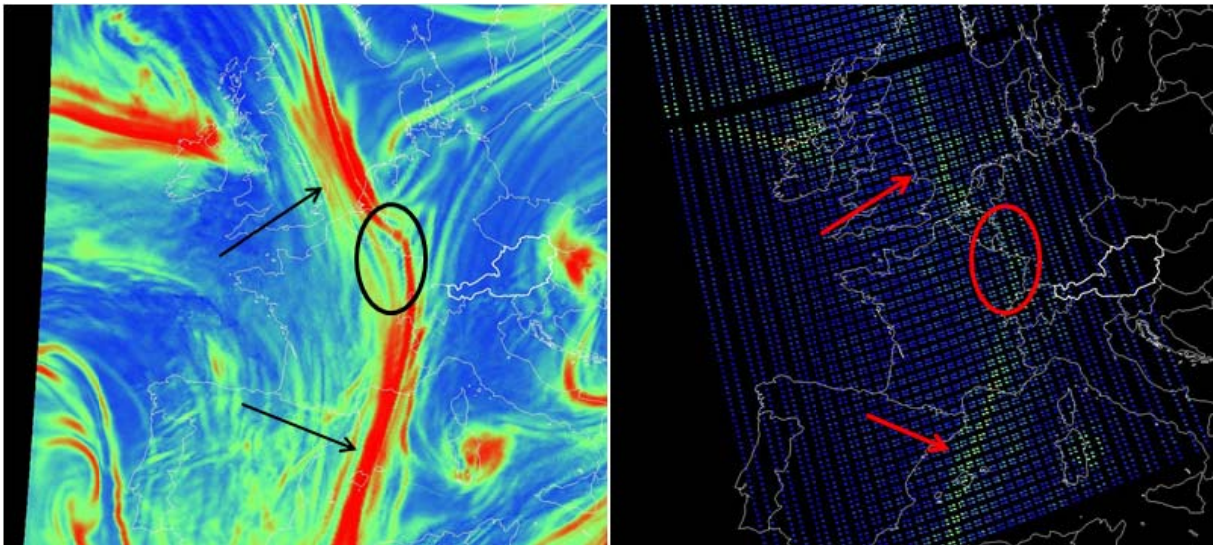

Figure 24: *Comparison of the IASI derived tropopause folds (right) with the ASII-TF output (left). Date: 26 March 2018, 20:45 UTC. High probabilities for being located at a tropopause fold are depicted in red in the ASII-TF product; high gradients of the tropopause height are depicted in green in the IASI output.*

Comparison of the obtained IASI tropopause folds with the output of the ASII-TF product was made by visual inspection. Generally, the two fields show a fairly good agreement of the position

of the tropopause folds. In **Figure 24**, the tropopause folding zone stretching in north-south direction across Europe can be seen in both products (red and black arrows); the same holds for the weaker gradient zone over eastern France and the Benelux countries (red and black circle).

In this example which is typical for many other examples, it can be seen that ASII-TF gives a more detailed picture of the tropopause folds than the IASI analysis. But both data sources show the same pattern regarding the location of the main tropopause folds.

Figure 25 provides an example for the fact that not only frontal areas, but also upper level lows are usually tightly connected to tropopause folds.

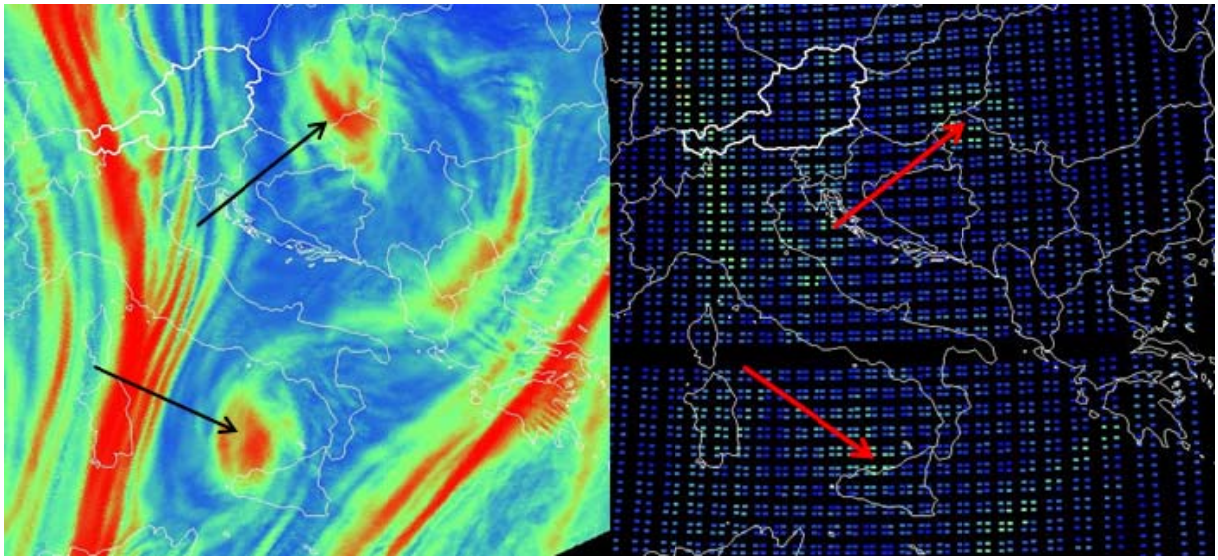

Figure 25: *Comparison of the IASI-derived tropopause folds (right) with the ASII-TF output (left). Date: 27 March 2018, 08:45 UTC. High probabilities for being located at a tropopause fold are depicted in red in the ASII-TF product; high gradients of the tropopause height are depicted in green in the IASI output.*

Both upper level low centers over Hungary/Serbia and the Thyrrhenian Sea are depicted in the ASII-TF product and in the IASI sounding data at the same positions. Water vapor gradients from the WV6.2µm channel are an input parameter to the ASII-TF product helping to locate the tropopause folds. These gradients also coincide with a lowering of the tropopause height typical for upper level lows and shown in the IASI data.

In case of extended convective activity, the ASII-TF product usually shows large areas with low probabilities for being located at a tropopause fold (see **Figure 22**). This is confirmed by the IASI data which show a uniform tropopause height in the area covered by the convective cells (see **Figure 26**).

The dry slot over the southern Adriatic Sea however marks an area with a well-defined tropopause fold (red arrows in **Figure 26**). This zone is also marked as a gradient zone in the IASI-derived tropopause height.

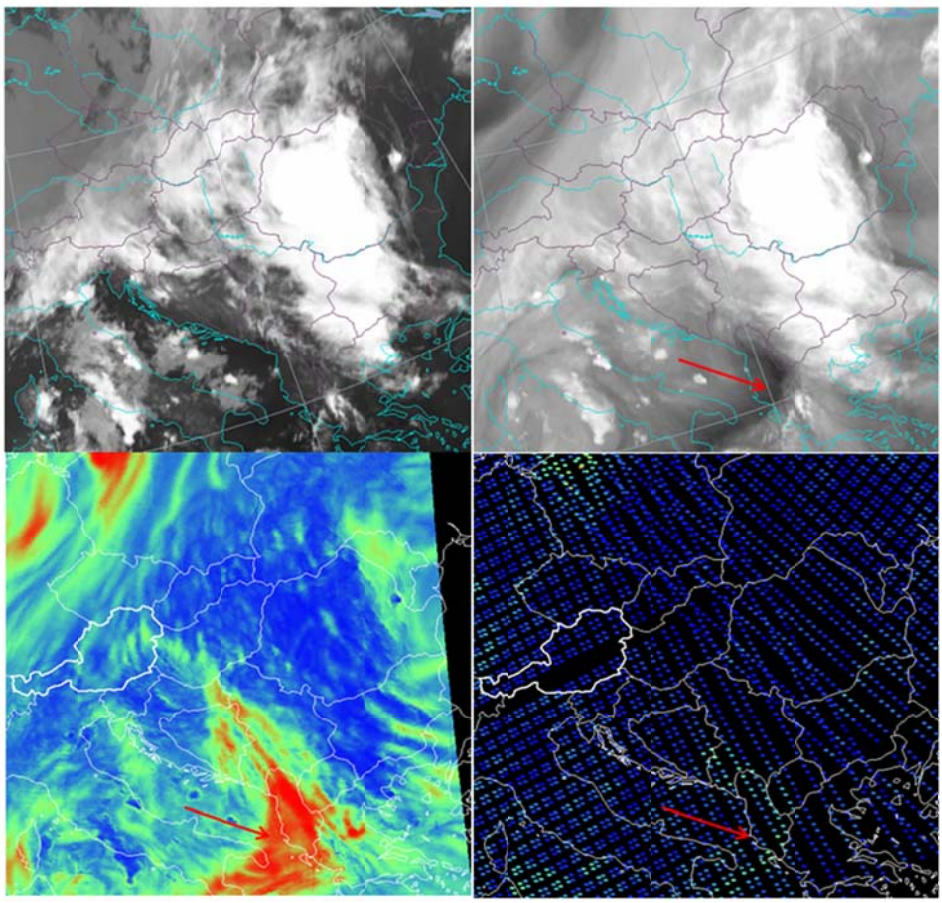

Figure 26: *Comparison of the IASI-derived tropopause folds (bottom right) with the ASII-TF output (bottom left). Date: 27 March 2018, 08:45 UTC. High probabilities for being located at a tropopause fold are depicted in red in the ASII-TF product; high gradients of the tropopause height are depicted in green in the IASI output. IR 10.8 µm (top left) and WV 6.2 µm (top right) images from Meteosat-11 show the position of the large convective cell.*

3.3 CASE STUDY: 16 APRIL 2018

The validation case of 16 April 2018 is presented here in some detail because on this day an unusually high number of PIREPs signaling moderate or severe turbulence were received by the Austrian Air Traffic Control (ACG).

3.3.1 Synoptic situation

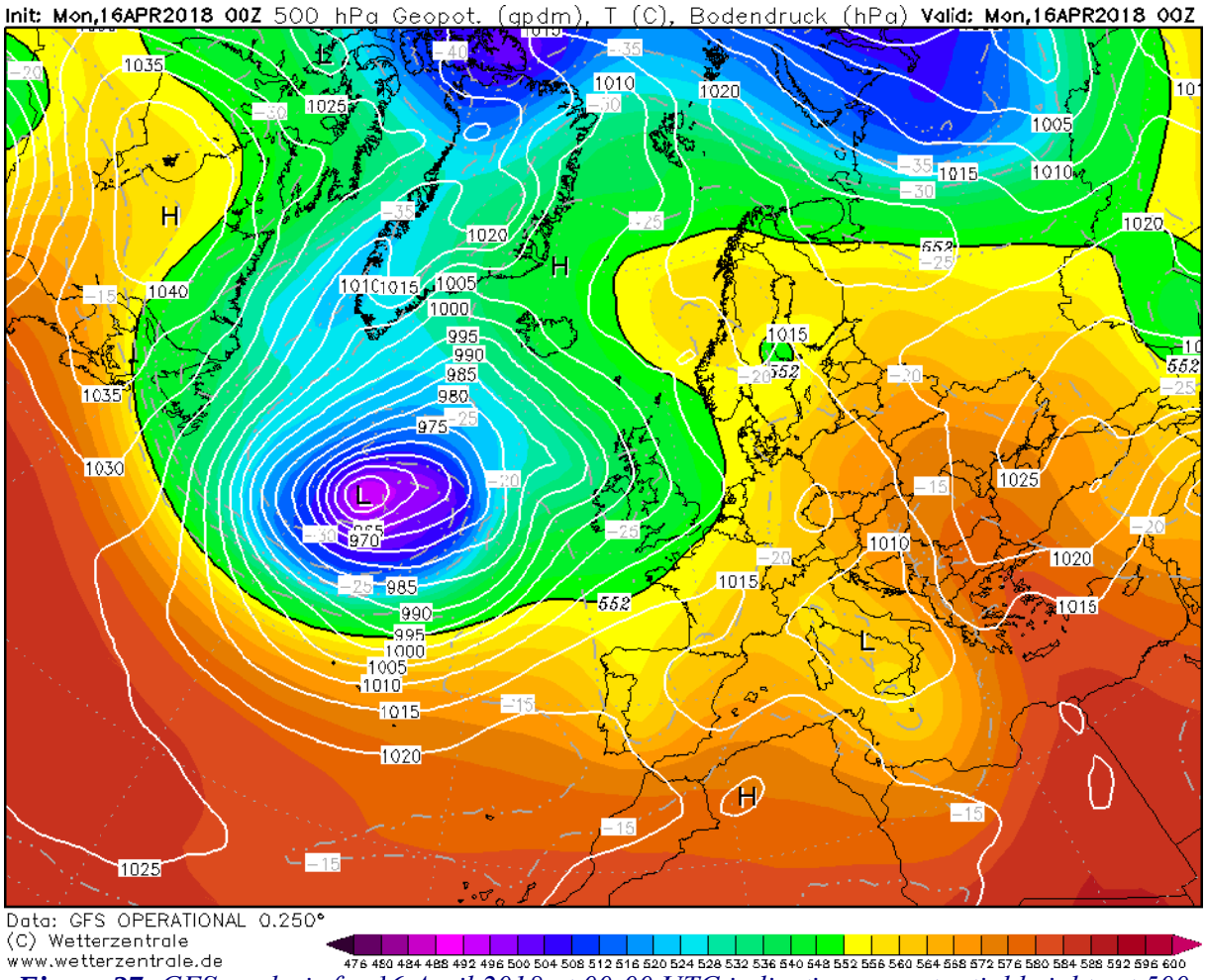

Figure 27: *GFS analysis for 16 April 2018 at 00:00 UTC indicating geopotential heights at 500 hPa and surface pressure (white).*

A narrow trough is located over the Italian peninsula, warm and moist unstable air masses are advected from the Adriatic Sea towards Croatia, Slovenia and the southern parts of Austria (see **Figure 27**). A stationary cold front extends in north-south direction over Central Europe (see **Figure 28**); a jet streak is located over the eastern flank of the trough extending from South Italy to Slovenia (see **Figure 29**). In the course of the day, severe thunderstorms develop over Slovenia. Our area of interest for the verification of the ASII-TF product will be the rear side of the stationary cold front extending from Slovenia and Austria to the Czech Republic (green circle in **Figure 28**).

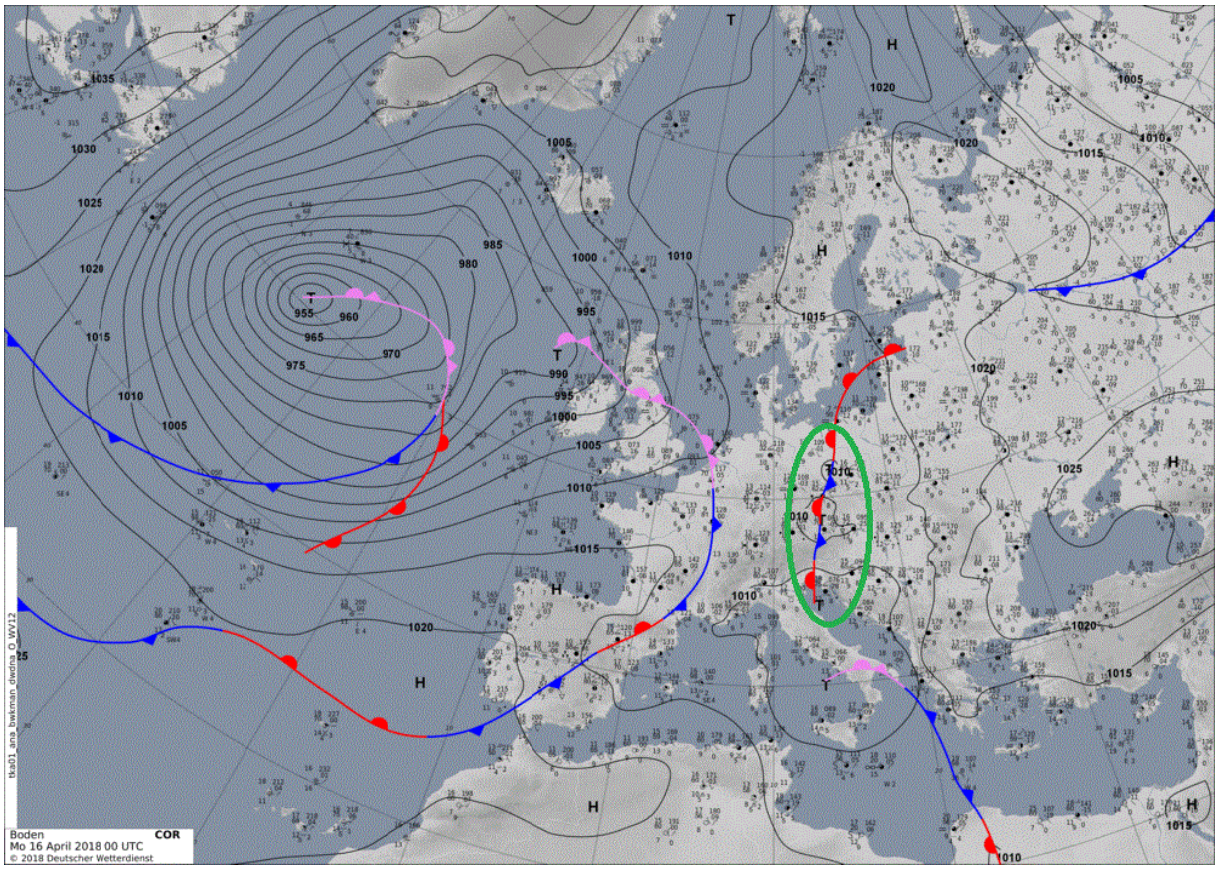

Figure 28: *DWD surface chart for 16 April 2018, 00:00 UTC. The area of interest is marked in green.*

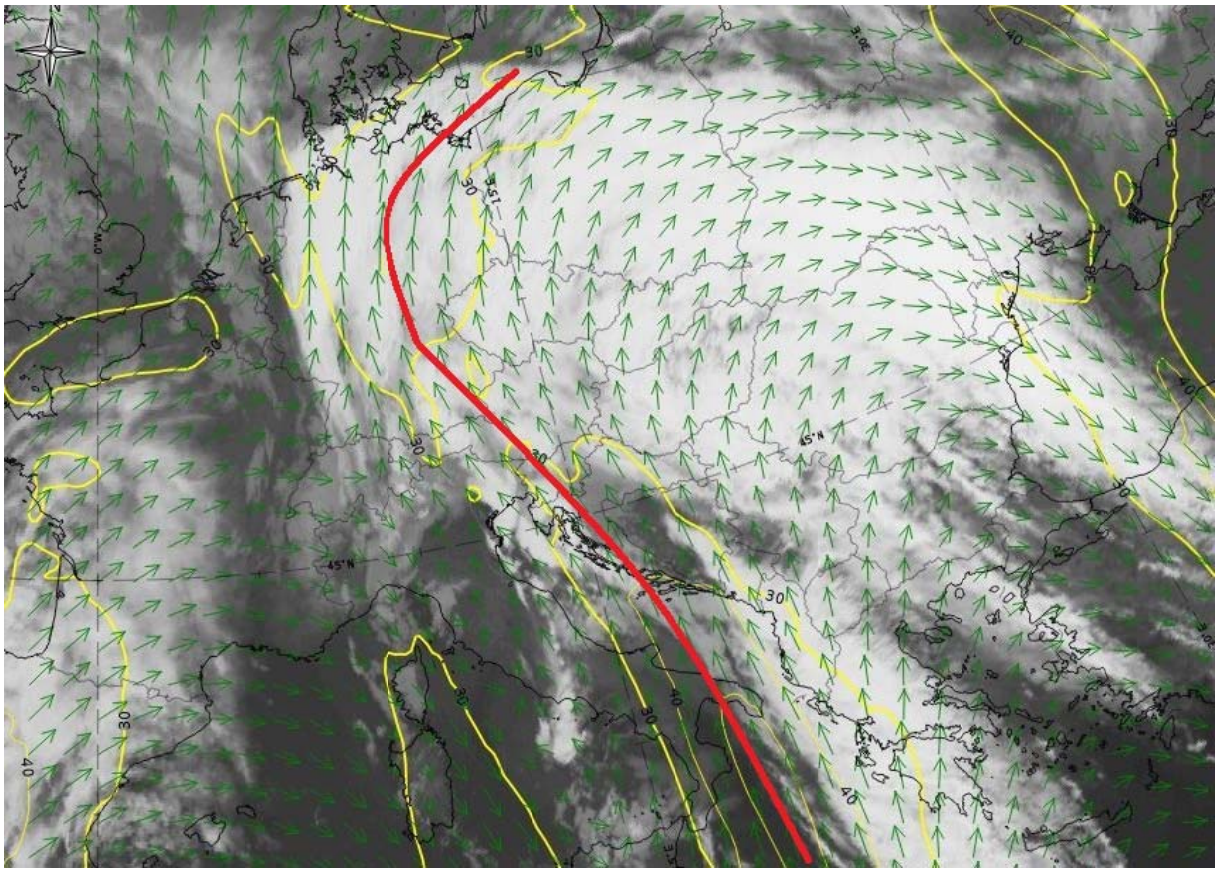

Figure 29: *IR10.8 µm satellite image from Meteosat-11 (16 April 2018, 00:00 UTC); isotachs at 300 hPa in yellow and wind direction in green. The red line marks the axis of the jet streak.*

3.3.2 Comparison of ASII-TF with IASI level 2 tropopause height

An overpass of the MetOp-B satellite at 08:50 UTC carrying the IASI instrument onboard allows a comparison of IASI tropopause analyses with the results of the ASII-TF product for 08:45 UTC. Both products show a good accordance in depicting the regions affected by a tropopause fold. The ASII-TF output shows high probability values for a tropopause folding on both sides of the narrow trough (North and Central Italy and from Croatia to Austria respectively). The back-side of the stationary cold front is shown in both products as tropopause fold; the red (ASII-TF) and green (IASI) line follows the axis of the jet (see **Figure 30** and **Figure 31**). Note that the tropopause fold over Germany visible in the ASII-TF product is hardly seen in the IASI output (see **Figure 30**). For this region, the ASII-TF product shows decreasing probabilities for being a tropopause fold in the course of the day.

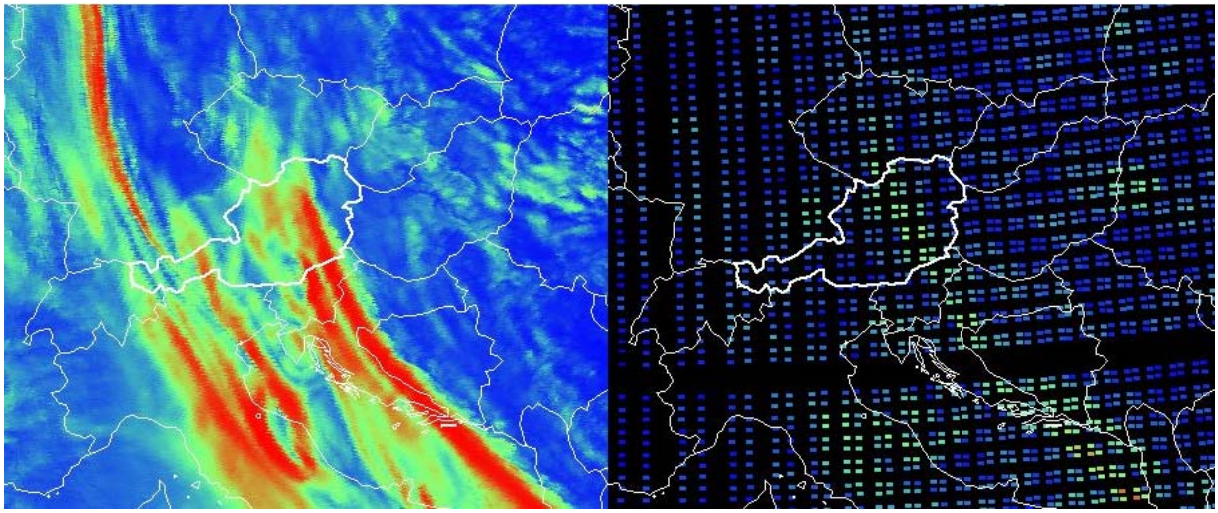

Figure 30: *Left: ASII-TF analysis for 16 April 2018, 08:45 UTC. Areas with a high probability for being located at a tropopause fold are marked in red. Right: Tropopause gradient from IASI sounding data for the same day at 08:50 UTC.*

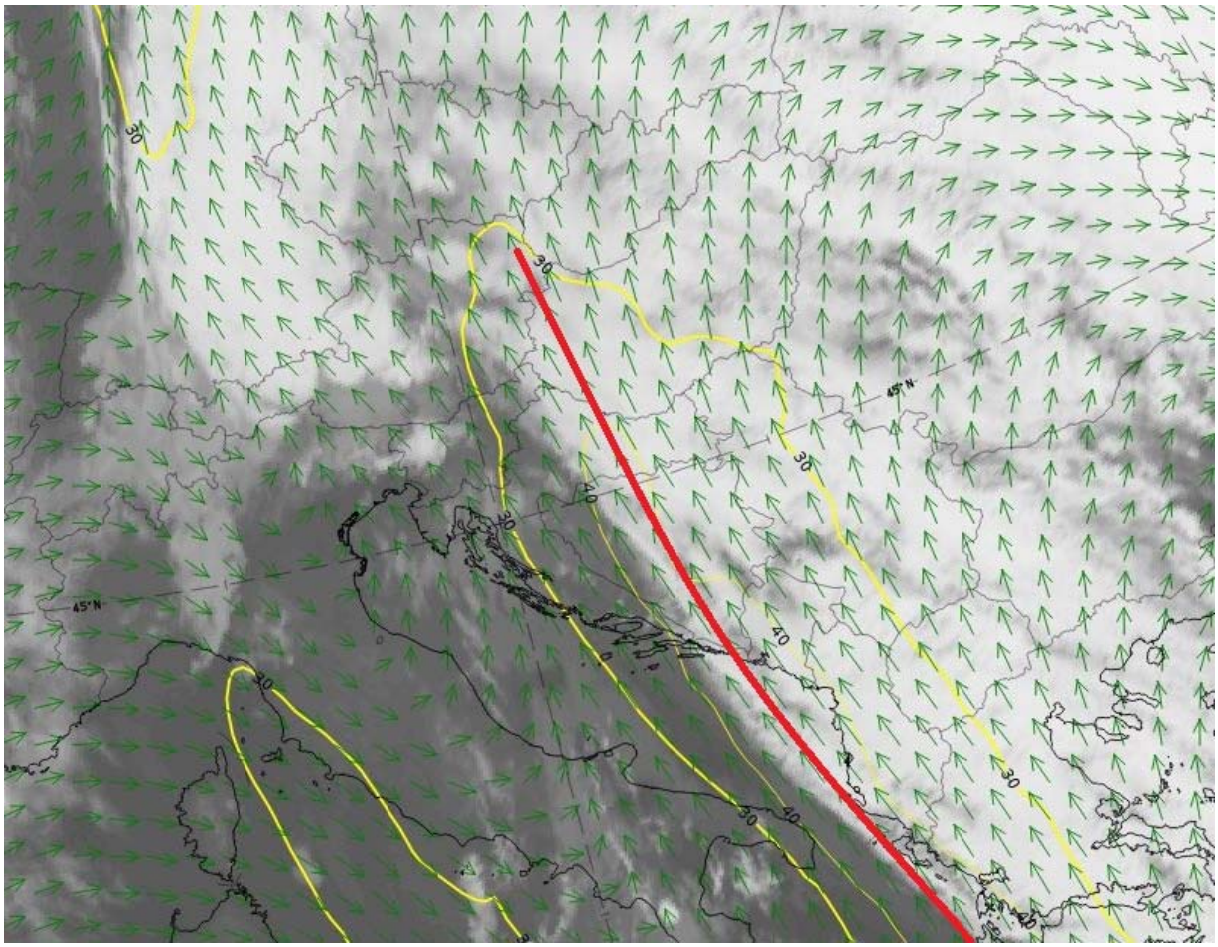

Figure 31: *IR10.8 µm satellite image from Meteosat-11 (16 April 2018, 06:00 UTC); isotachs at 300 hPa in yellow and wind direction in green. The red line marks the axis of the jet streak.*

3.3.3 Evaluation of the PIREPs (16 April 2018)

PIREPs reporting moderate and heavy turbulence within or next to the Austrian air space have been issued between 12:15 and 15:58 UTC on 16 April 2018 by pilots of affected airplanes. As the cold front over Austria is nearly stationary, the position of the tropopause folding observed in the IASI overpass at 8:50 UTC is also valid for the investigated time frame 12:00 – 16:00 UTC.

The first 3 turbulence reports were issued around 12:15 UTC from an Airbus A319 and 2 not further specified "heavy" airplanes. All turbulence reports are located in direct vicinity to the areas labeled with high probabilities for showing strong gradients of the tropopause height in the ASII-TF product (see **Figure 32**). Two of the reports are located at the same position over the southern part of Austria but issued for different flight levels, the other PIREP is located over Pardubice Airport (Czech Republic). Strong vertical wind shear is observed at both locations at the indicated flight levels (around 220 hPa) induced by a jet streak with a north to south axis (see **Figure 31** and **Figure 33**).

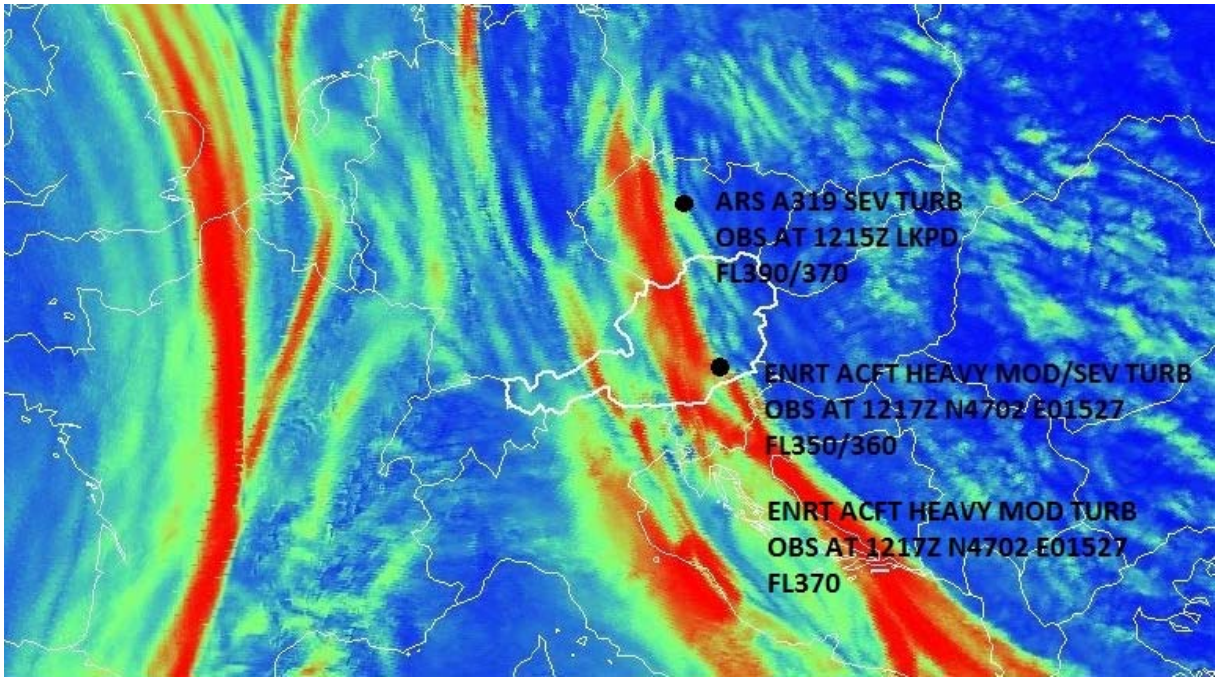

Figure 32: *Detail of the ASII-TF product for 16 April 2018, 12:15 UTC. Areas with a high probability for being located at a tropopause fold are marked in red. PIREPS and their exact locations are marked in black.*

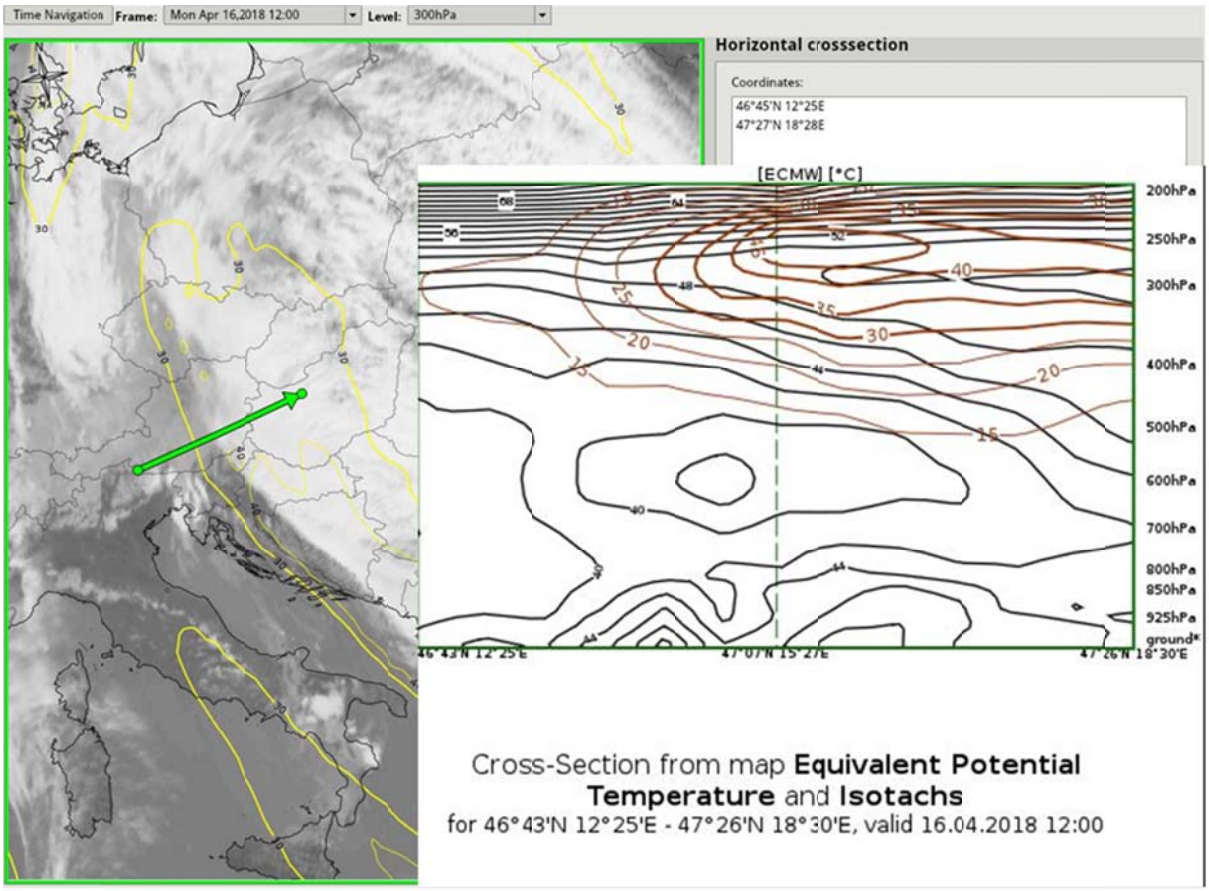

Figure 33: *16 April 2018, 12:00 UTC: Vertical cross section through the area of the reported turbulence. The position of the cross section is marked in green; isotachs at the 300 hPa level are depicted in yellow.*

The next two turbulence reports were issued over the eastern part of Slovenia at 13:11 and 14:00 UTC respectively. Both PIREPs locate the experienced turbulence within the highest values of the tropopause folding probability of the ASII-TF product (see **Figure 34** and **Figure 35**). The reported position corresponds to the rear side of the frontal cloud band of a stationary cold front; this is also the position of high wind shear at the indicated flight level (FL390 and FL380 respectively). Developing thunderstorms do not yet affect this area as can be seen in **Figure 36**.

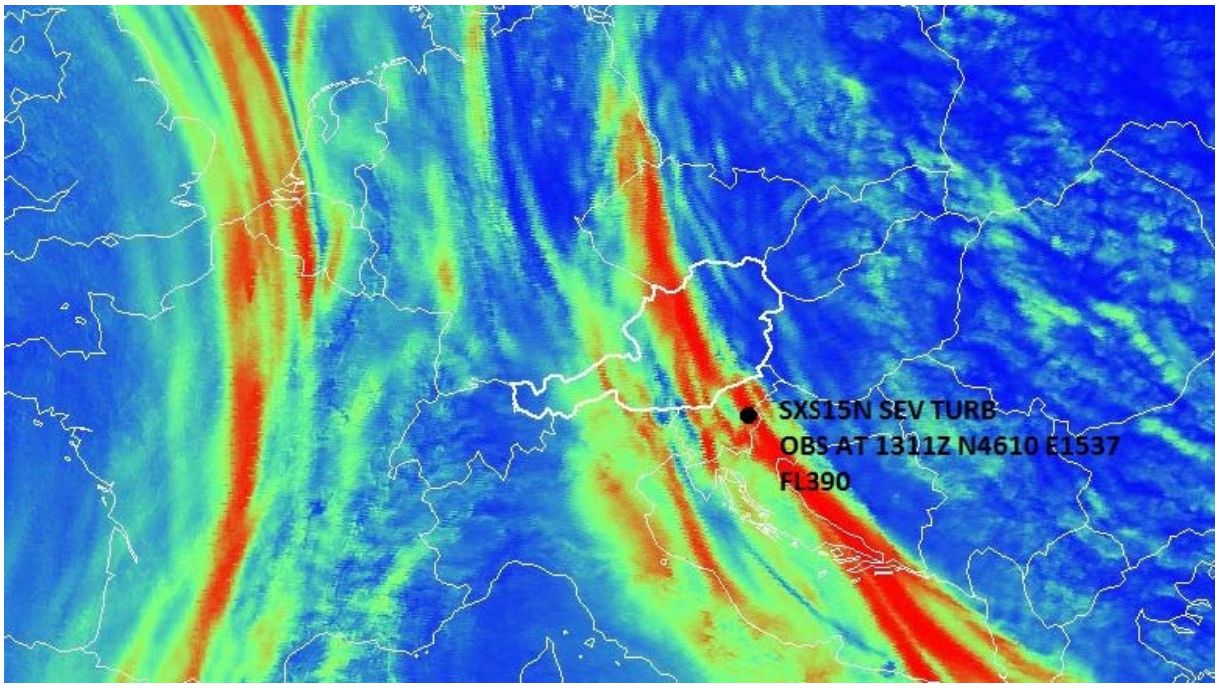

Figure 34: *Detail of the ASII-TF product for 16 April 2018, 13:15 UTC. Areas with a high probability for being located at a tropopause fold are marked in red. PIREPS and their exact locations are marked in black.*

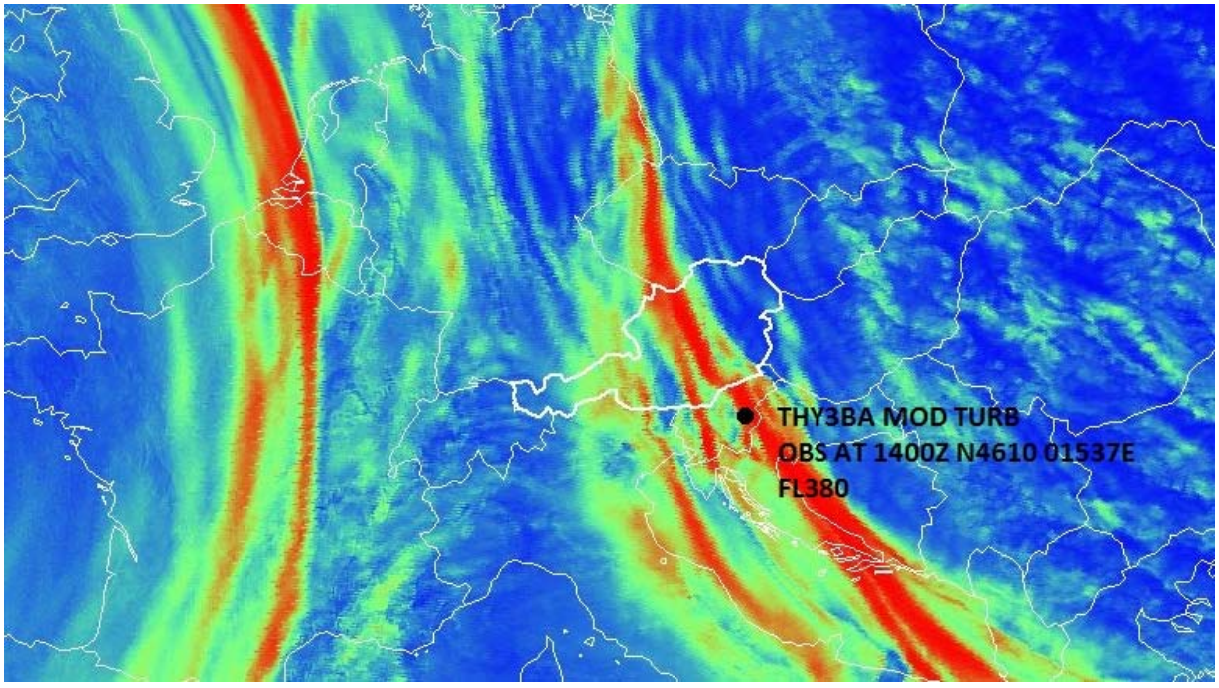

Figure 35: *Detail of the ASII-TF product for 16 April 2018, 14:00 UTC. Areas with a high probability for being located at a tropopause fold are marked in red. PIREPS and their exact locations are marked in black.*

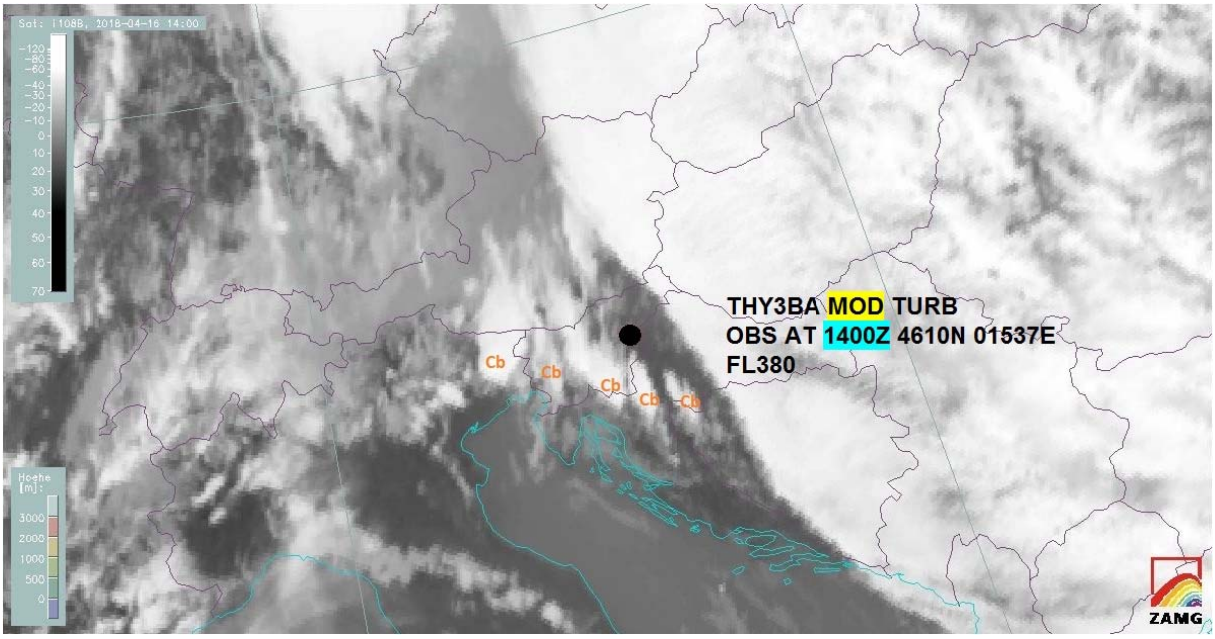

Figure 36: *IR 10.8 µm image from Meteosat-11 (16 April 2018, 14:00 UTC). The black dot marks the area of the reported turbulence, developing Cumulonimbus clouds are indicated by orange Cb tags.*

Around 14:30 UTC, three more turbulence reports were issued by pilots of passenger airplanes crossing the tropopause folding zone depicted in the ASII-TF product (see **Figure 37**). All of them crossed the red region of high probability (> 67%) for being a tropopause fold at FL370 (~220 hPa) which corresponds to the upper jet level with strong vertical wind shear. Although convective developments further increased over Slovenia, none of the turbulence reports were related to convective activity.

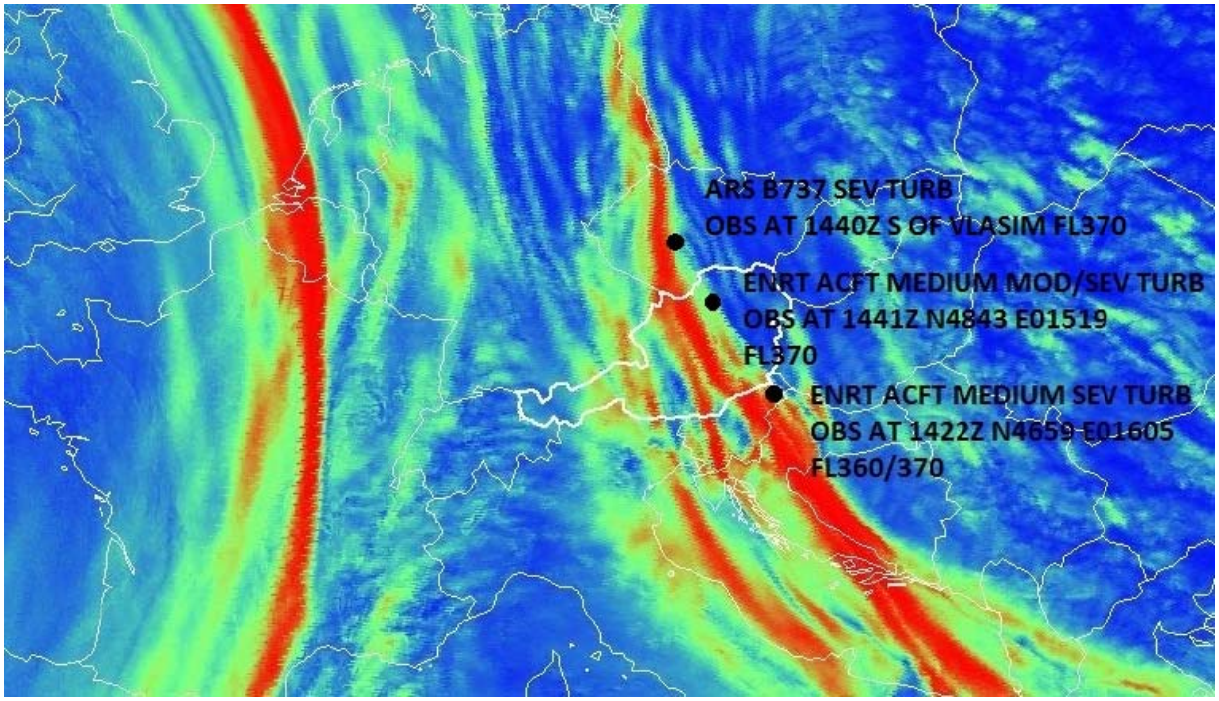

Figure 37: *Detail of the ASII-TF product for 16 April 2018, 14:30 UTC. Areas with a high probability for being located at a tropopause fold are marked in red. PIREPS and their exact locations are marked in black.*

The next turbulence warning was issued at 15:34 UTC by a Boeing 777 flying over eastern Germany near the border to Poland. The location of the reported turbulence is exactly within a probability maximum of the ASII-TF product (**Figure 38**).

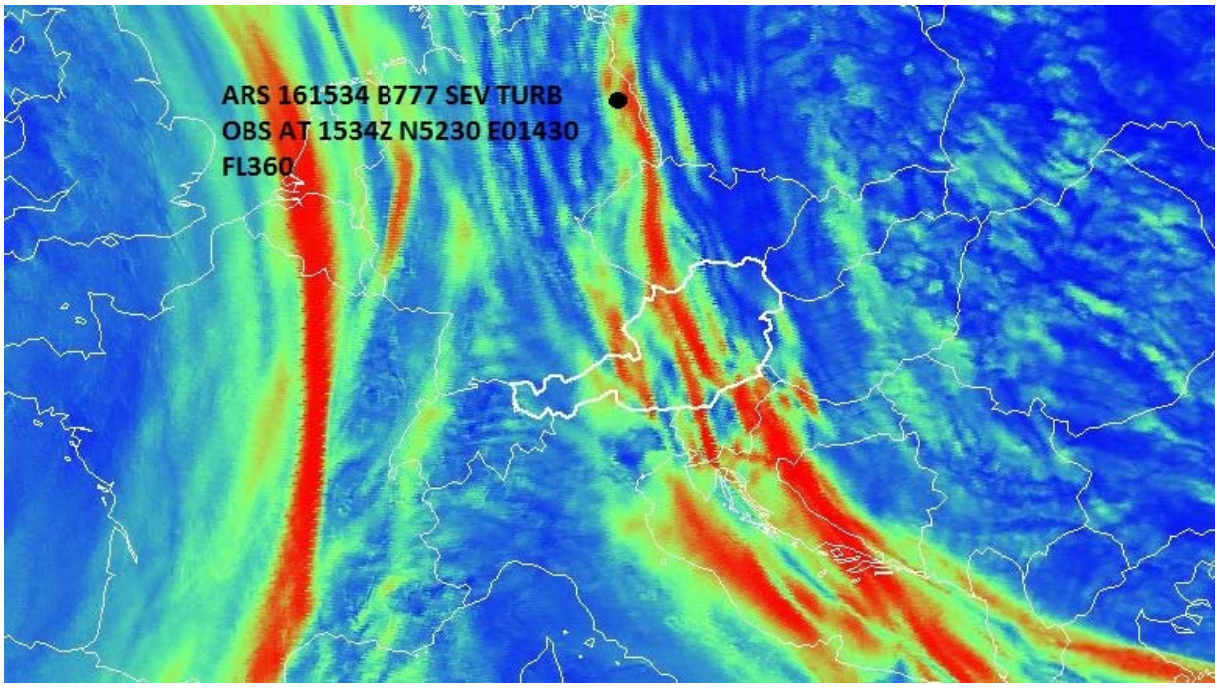

Figure 38: *Detail of the ASII-TF product for 16 April 2018, 15:30 UTC. Areas with a high probability for being located at a tropopause fold are marked in red. PIREPS and their exact locations are marked in black.*

The last turbulence report within this time span nevertheless came from a region identified as an area with low probabilities (blue) for being located at a tropopause folding zone (**Figure 39**). This turbulence report was issued at 16:00 UTC over Vienna and it reports moderate to severe turbulence at flight level 380. The model analysis shows strong wind shear at FL380 above Vienna which is obviously the reason for the observed turbulence (**Figure 41**).

At 16:00 UTC, Vienna is covered by high reaching frontal cloudiness (up to 10 000 meter) and precipitation is falling (**Figure 40**). Cloud tops are located below the indicated flight level.

Model fields indicate a jet streak located over the eastern part of Austria with strong vertical wind shear between 250 and 200 hPa (**Figure 41**).

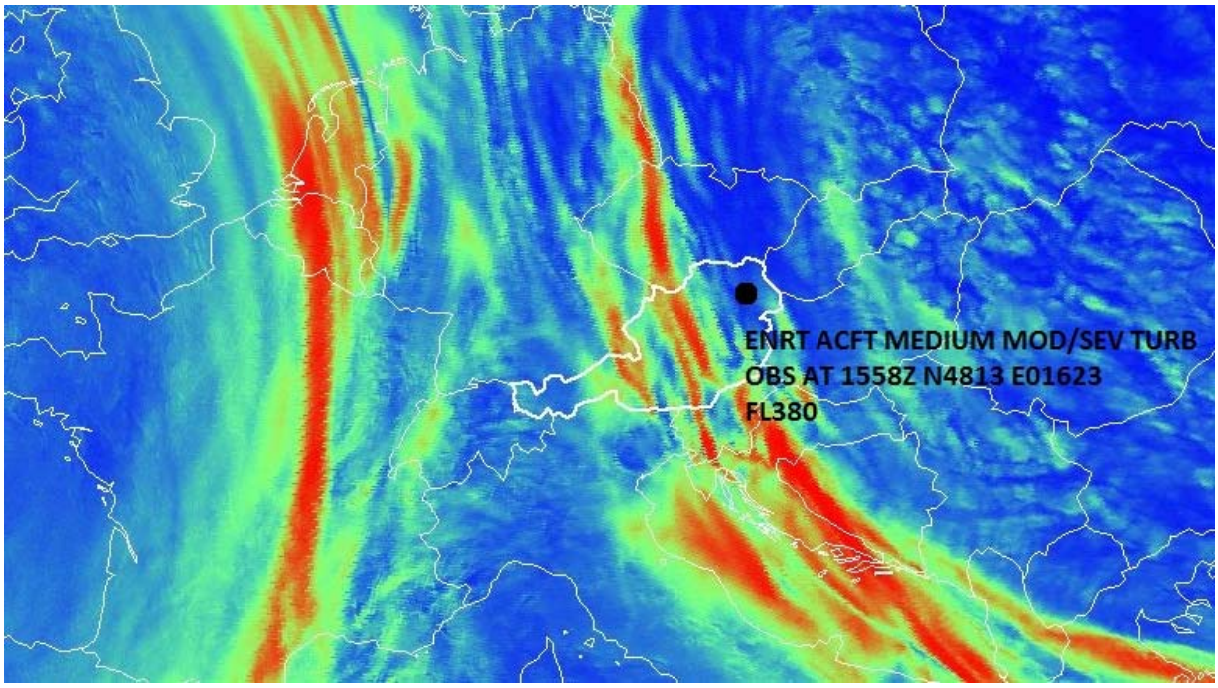

Figure 39: *Detail of the ASII-TF product for 16 April 2018, 16:00 UTC. Areas with a high probability for being located at a tropopause fold are marked in red. PIREPS and their exact locations are marked in black.*

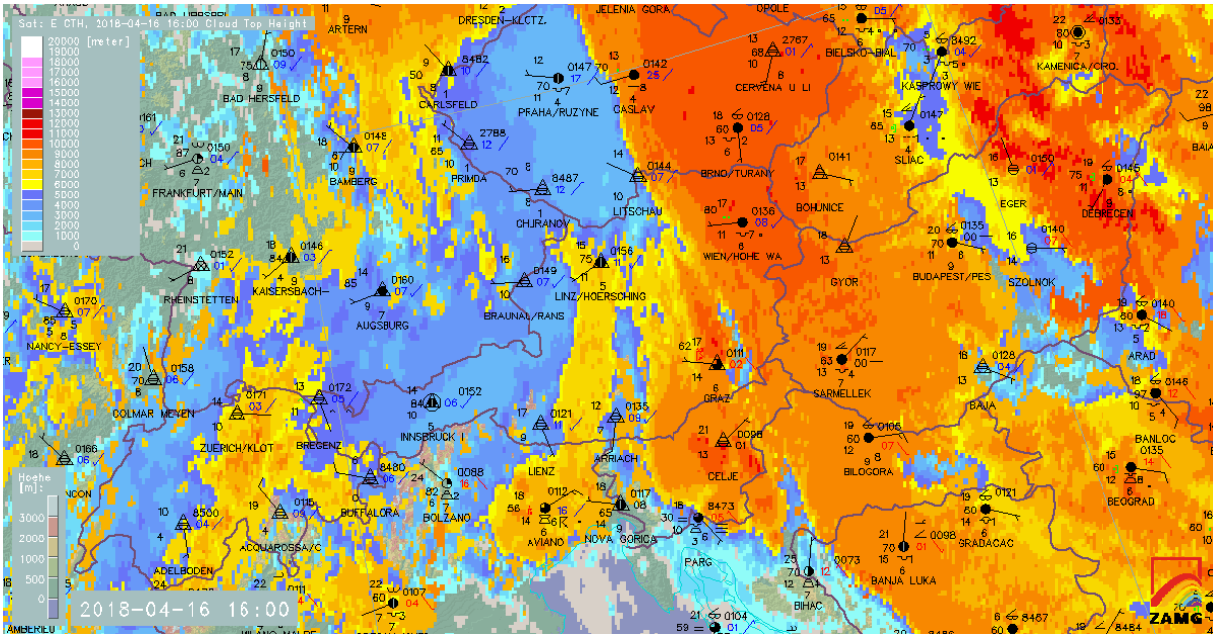

Figure 40: *NWCSAF Cloud top height and surface weather reports from 16 April 2018 at 16:00 UTC.*

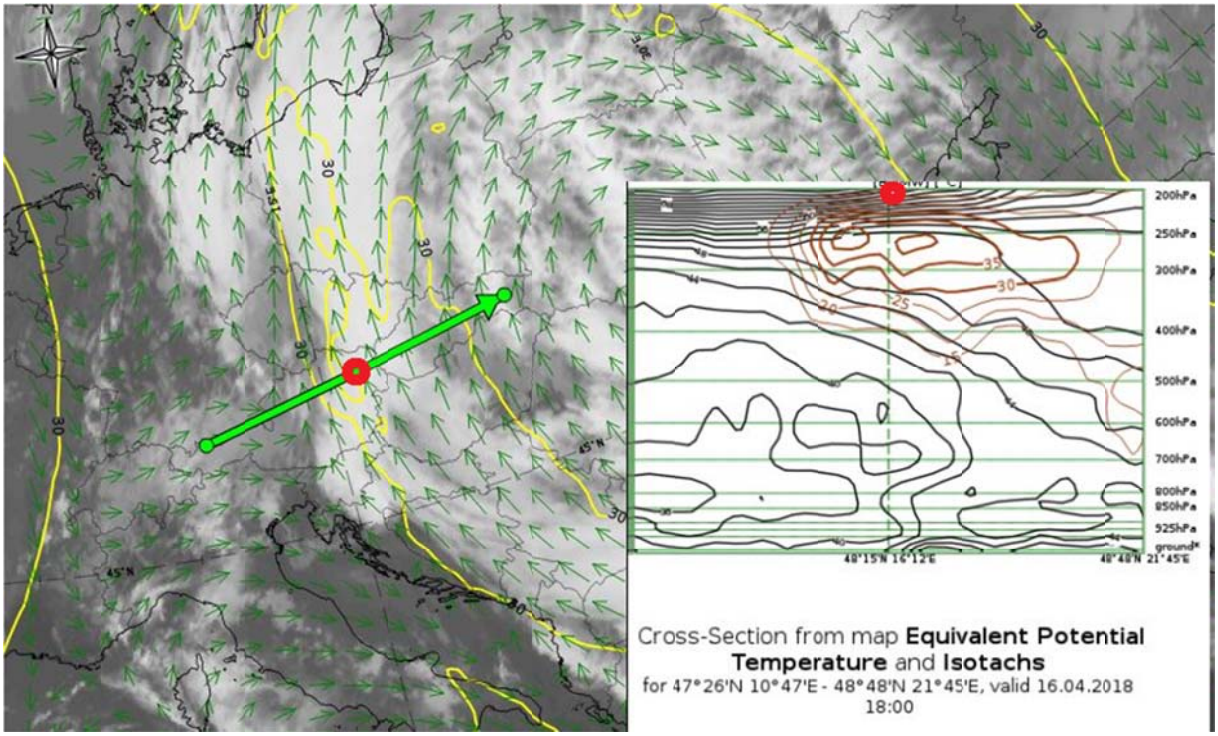

Figure 41: *16 April 2018, 18:00 UTC: Vertical cross section through the area of the reported turbulence. The red circles indicate the location of the reported moderate to severe turbulence.*

3.4 CONCLUSIONS

Turbulence warnings from PIREPs have been chosen to validate the ASII-TF product in view of its ability to localize the occurrence of turbulence in the atmosphere. Acknowledging the deficiencies of this validation approach (elaborated, for example, by Brown and Young, 2000), the validation results still confirm a close relation between turbulence caused by wind shear and the presence of tropopause folds. Nevertheless, it should be kept in mind that turbulence caused by wind shear is only indirectly related to tropopause folds via the existence of horizontal temperature gradients which on their side are directly linked to the existence of jet streams. Although ASII-TF includes shear vorticity and wind speed at 300 hPa, the product has been tuned to identify the narrow lines of tropopause folds. If the ASII-TF product is intended to be used as a turbulence forecasting tool, the adjacent regions with high wind shear at and near jet streaks should be considered additionally. This is in accordance with investigations by Knox et al. (2006).

Comparison of the ASII-TF product with IASI-derived tropopause gradients showed a good positional agreement. Visual inspection of the ASII-TF product shows that the latter depicts more details of the gradient structure and seems more sensitive to weaker gradients than the IASI level 2 product. The case study at the end of the validation report compares turbulence reports with ASII-TF probabilities for 16 April 2018. Most severe turbulence reports are located within the region of high ASII-TF probabilities for being located at a tropopause fold. This case study also confirms the results from the PIREP cases that recorded turbulence is closely related to jet streaks which are the main source of turbulence.

3.5 REFERENCED SCIENTIFIC PUBLICATIONS

Brown, B.G., and G.S. Young (2000): Verification of icing and turbulence forecasts: Why some verification statistics can't be computed using PIREPS. 9th Conference on Aviation, Range, and Aerospace Meteorology, Orlando, FL, 11-15 September 2000, 393-398.

Ellrod, G.P., and D.J. Knapp (1992): An Objective Clear-Air Turbulence Forecasting Technique: Verification and Operational Use. Weather and Forecasting, Vol. 7, 150-165.

Knox, J.A., Ellrod, G.P., and P.D. Williams (2006): Improved Clear Air Turbulence Diagnostics Based on Adjustment Dynamics, 12th Conference on Aviation Range and Aerospace Meteorology, 2006, https://ams.confex.com/ams/Annual2006/webprogram/Paper101397.html (accessed in September 2018)

Robichaud, A. (2006). A case study of a remarkable tropopause folding over Eastern North America on March 14-15 2006. 10.13140/RG.2.1.1000.2806, https://www.researchgate.net/publication/303053095/download (accessed in September 2018)

Sharman, R., Tebaldi, C., Wiener, G., and J. Wolff (2006): An Integrated Approach to Mid- and Upper-Level Turbulence Forecasting, Weather and Forecasting, Vol. 21, pp. 268-287.

Vieira, A. (2005): Mountain Wave Activity Over the Southern Rockies, Albuquerque Center Weather Service Unit (CWSU), https://www.weather.gov/media/abq/LocalStudies/MountainWavesUpdate.pdf (accessed in September 2018)

Wimmers, A., and W. Feltz (2006), Observing clear air turbulence indirectly in satellite imagery, Paper P8.1 presented at 12th Conference on Aviation and Aerospace Meteorology, Am. Meteorol. Soc., Atlanta, Ga. https://ams.confex.com/ams/pdfpapers/100701.pdf